‘Off-pore’ nucleoporins relocalize heterochromatic breaks through phase separation

Chiara Merigliano[1], Taehyun Ryu[2], Colby D. See[1], Christopher P. Caridi[1], Nadejda Butova[1], Trevor Reynolds[1], Changfeng Deng[3], David M. Chenoweth[3], Maya Capelson[4], Irene Chiolo[1*]

[1]University of Southern California, Molecular and Computational Biology Department, Los Angeles, CA, USA
[2]Harvard Medical School, Department of Genetics, Boston, MA, USA
[3]University of Pennsylvania, Department of Chemistry, School of Arts and Sciences, Philadelphia, PA, USA
[4]San Diego State University, Department of Biology, San Diego, CA, USA

*Correspondence: chiolo@usc.edu

Highlights

- Nup88, Nup98 and Sec13 are required for relocalization of heterochromatic DSBs
- Nup88 and Sec13 independently recruit Nup98 to DSBs downstream from Smc5/6
- Nup98 promotes relocalization and excludes Rad51 from the heterochromatin domain
- Phase separation by Nup98 is required and sufficient for relocalization and Rad51 exclusion

Summary

Heterochromatin mostly comprises repeated DNA sequences prone to ectopic recombination. In *Drosophila* cells, ‘safe’ homologous recombination (HR) repair of heterochromatic double-strand breaks (DSBs) requires relocalization of repair sites to the nuclear periphery before Rad51 recruitment and strand invasion. Relocalization is driven by nuclear actin filaments and myosins, while anchoring is mediated by the Nup107 complex at nuclear pores. Here, we show an additional ‘off pore’ role of nucleoporins in heterochromatin repair. Sec13 and Nup88 independently recruit Nup98 to DSBs before relocalization and downstream from the Smc5/6 complex and SUMOylation. Remarkably, the phase separation properties of Nup98 are required and sufficient to induce the mobilization of repair sites and to exclude Rad51, thus preventing aberrant recombination while facilitating HR repair. Disrupting this pathway results in heterochromatin repair defects, revealing a novel role for nucleoporins and phase separation in nuclear dynamics and genome integrity in a multicellular eukaryote.

Keywords

Heterochromatin repair, homologous recombination, DNA double-strand break repair, repair dynamics, nuclear dynamics, phase separation, condensates, Nup88, Nup98, Sec13.

INTRODUCTION

Specialized mechanisms promote HR repair in pericentromeric heterochromatin (hereafter 'heterochromatin') while preventing aberrant recombination [1-4]. Heterochromatin comprises ~10-30% of human and fly genomes [5], and is mostly composed of repeated DNA sequences (*e.g.,* transposons, and 'satellite' repeats [6, 7]), and 'silent' epigenetic marks (*e.g.*, H3K9me2/3 and HP1 [8]). In heterochromatin, thousands to millions of identical repeated sequences, including those from different chromosomes, can engage in ectopic recombination, presenting a serious threat to genome stability in multicellular eukaryotes [9].

In *Drosophila* cells, where heterochromatin forms a distinct nuclear domain [8, 10, 11], aberrant recombination is prevented by a dedicated pathway that relocalizes DSBs to the nuclear periphery before Rad51 recruitment and strand invasion [10, 12, 13]. Relocalization likely prevents aberrant recombination by isolating damaged DNA from similar repeated sequences on non-homologous chromosomes, thus promoting 'safe' exchanges with sister chromatids or homologs [1, 2, 10, 12-16]. A similar relocalization occurs in mouse cells [13, 17-19], demonstrating conserved pathways.

Key elements of this pathway include a transient network of nuclear actin filaments (F-actin) that mediate nuclear myosin-driven relocalization through directed motions [13]. Notably, filaments and directed motions are mostly detected between the heterochromatin domain periphery and the nuclear periphery [13], raising the question of how heterochromatic breaks reach the heterochromatin domain periphery in the first place. Additionally, SUMOylation by dPIAS and the Smc5/6 subunits Nse2/Cerv and Nse2/Qjt also mediate relocalization and establish the block to HR progression inside the heterochromatin domain [10, 12, 13, 15], although the downstream effectors of this regulation remain largely unknown.

At the nuclear periphery, anchoring of repair sites to the pores relies on the nucleoporin Nup107, and this anchoring is required for restarting repair via Brca2/Rad51 recruitment [12]. Nucleoporins also have chromatin-associated functions independent of the pores [20-24]. Specifically, *Drosophila* Nup88, Nup98 and Sec13 are recruited to gene promoters in the nucleoplasm to activate transcription during fly development [20, 21]. Whether these components contribute to other chromatin responses is unknown, and a direct role in DSB repair has never been described.

Notably, nucleoporins are frequently misregulated in cancer. Nup88 overexpression is an important cancer biomarker [25, 26], while Nup98 is a component of over 30 different fusion oncoproteins responsible for leukemias [27], particularly childhood malignancies with poor prognoses [27]. Thus, understanding the roles of these components in DNA repair is essential to establishing how their misregulation can contribute to genome instability and tumorigenesis, as well as for developing better therapeutic approaches.

Here, we show that Nup88, Nup98 and Sec13 nucleoporins are recruited to heterochromatic DSBs downstream from Smc5/6 to mediate relocalization of repair sites, DNA repair focus clustering, and Rad51 exclusion. The nucleoplasmic fraction of these nucleoporins, and not their role at the nuclear periphery, is responsible for these functions. Remarkably, Nup98-dependent phase separation is required and sufficient for mobilizing repair sites inside the heterochromatin domain and for preventing Rad51 recruitment and aberrant recombination in heterochromatin. Together, these studies reveal a novel 'off-pore' function of nucleoporins in heterochromatin stability, nuclear dynamics, and genome integrity.

RESULTS

Nup88, Nup98 and Sec13 are required for relocalizing heterochromatic DSBs

In *Drosophila* cells, repair sites leave the heterochromatin domain starting 10 min after DSB induction with ionizing radiation (IR), resulting in fewer repair sites (γH2Av foci) in DAPI-bright heterochromatin 60 min after IR [10, 12, 13]. In the absence of Nup107, defective anchoring to the nuclear periphery results in break sites returning to the heterochromatin domain, leading to a higher number of γH2Av foci in the DAPI-bright region 60 min after IR without affecting total focus count [10, 12, 13].

We previously established that other nucleoporins facing the nucleoplasmic side of the pore (*i.e.,* Nup205, Nup50 and Nup93) do not affect relocalization of repair sites, consistent with a specialized role for Nup107 in anchoring. We tested additional nucleoporins that are known to interact with chromatin [20, 21, 28] (Figure 1A). RNAi depletion of Nup88 and Sec13 (Figure 1B and Figure S1A), but not of Nup62 or Elys (Figure 1B and Figure S1A), results in a higher number of γH2Av foci in DAPI-bright 60 min after IR, consistent with relocalization defects. Nuclear pore organization at the nuclear periphery is not affected by these RNAi conditions (Figure S1E). Notably, Nup88 and Sec13 are among the few nucleoporins identified for their nucleoplasmic function in transcription regulation, independent from their role at the pore [20, 21, 28] (Figure 1A). Nup214 and Nup358, which closely interact with Nup88 to mediate its function at the pore [29-32], are not required for relocalization (Figure S1A-D), suggesting a function of Nup88 independent from its role at the pore.

Next, we tested the role of Nup98, another nucleoporin working both on- and off-pore (Figure 1A), which is generated from proteolysis of the Nup98-96 peptide [33]. Nup98 RNAi results in co-depletion of Nup96 and destabilization of the Y complex it belongs to, indirectly affecting Nup107 association with the pore. To test the role of Nup98 independently from Nup96 and Nup107, we RNAi depleted Nup98 while exogenously expressing Nup96, which restores stability of the Y complex and Nup107 association with the nuclear pores (Figure S1F). In these conditions, Nup98 RNAi results in persistent γH2Av foci in DAPI-bright 60 min after IR, consistent with a role for Nup98 in relocalizing heterochromatic DSBs (Figure 1C).

Nup88, Nup98 and Sec13 could be required for relocalization by acting in the nucleoplasm, *i.e.* off-pore. Accordingly, Nup88, Nup98, and Sec13 become more associated with the chromatin starting 10 min after IR (Figure 1D and Figure S1G). These nucleoporins are also enriched at repair foci in triton-extracted samples that highlight chromatin-associated proteins (Figure 1E and Figure S1H). Co-localization with damage sites is observed in DAPI-bright starting 10 min after IR (Figure 1E and Figure S1H) *i.e.,* before relocalization [10, 12, 13]. RNAi depletion of Nup88, Nup98, or Sec13 results in loss of the corresponding signals at damage foci (Figure S2A), confirming the staining specificity. Most nucleoporin-enriched repair foci are also associated with heterochromatic epigenetic marks (Figure S2B), consistent with a role for Nup88, Nup98, and Sec13 at heterochromatic DSBs. We concluded that Nup88, Nup98, and Sec13 are required for relocalization of heterochromatic DSBs, and that they are recruited to heterochromatic DSBs before relocalization.

The nucleoplasmic fractions of Nup88, Nup98 and Sec13 are required for relocalization

We directly tested the possibility that Nup88, Nup98, and Sec13 contribute to the relocalization of heterochromatic DSBs off-pore by investigating the impacts of eliminating the nucleoplasmic fractions of these proteins on heterochromatin repair. We expressed Nup88, Nup98 or Sec13 fused to the integral membrane nucleoporin Ndc1, which constitutively targets proteins to the nuclear pore [34] (Figure 2A-C). Simultaneously, we RNAi depleted endogenous Nup88, Nup98 or Sec13 using siRNAs against their UTRs (Figure 2A-C and Figure S1A and S3A). Eliminating the nucleoplasmic fraction of Nup88, Nup98 or Sec13 through Ndc1 fusions results in major defects in relocalization of heterochromatic DSBs (Figure 2A-C, and Figure S3B-D), while expression of the corresponding wild-type nucleoporins in the same conditions restores normal relocalization (Figure S3E-G). This supports the importance of the nucleoplasmic fraction of Nup88, Nup98 or Sec13 in relocalization of heterochromatic DSBs.

As a complementary approach, we generated cells expressing 'nucleoplasmic-only' versions of Nup88, Nup98 or Sec13, for which mutations that specifically disrupt anchoring to the pores without affecting pore integrity were previously described [21, 35, 36]. As previously shown, removal of the C-terminal domain of Nup88 (Nup88ΔC) or Nup98 (Nup98FG) results in release of these proteins from the pores and loss of signal at the nuclear periphery [21, 36, 37] (Figure S4A-C). Similarly, expression of a Nup96ΔN mutant in the absence of endogenous Nup96, which loses the nuclear pore anchoring domain for Sec13 (Figure S4A, D-F), results in release of Sec13 from the nuclear periphery (Nup96 RNAi, Figure 3C). In all these conditions, recruitment of Nup88ΔC, Nup98FG, and Sec13 (in Nup96ΔN-expressing cells) to repair foci was not affected (Figure 1E and S4G), consistent with functional nucleoplasmic fractions of these nucleoporins. Importantly, in conditions where endogenous nucleoporins were RNAi depleted while nucleoplasmic-only nucleoporins were expressed, relocalization of heterochromatic DSBs occurs normally, *i.e.* similarly to cells expressing endogenous nucleoporins (Figure 3A-C and Figure S4B-C, F).

Notably, Nup88, Nup98 or Sec13 RNAi or Ndc1 fusions could affect nuclear pore transport, with indirect effects on relocalization of heterochromatic DSBs. We tested this by measuring nucleoplasmic protein transport with a light-inducible nuclear export system (LEXY) [38] (Figure S5A-B), which can detect both import and export defects. Treatment with Kpt-276 or Importazol, which inactivate nuclear pore export and import respectively, results in significant transport defects of the LEXY construct (Figure S5C), confirming the ability of this optogenetic tool to measure nucleoplasmic transport in fly cells. Transport through the nuclear pore is largely unaffected by Nup88 or Nup98 RNAi or Ndc1 tagging, suggesting that the defects in relocalization of heterochromatic DSBs observed in these conditions are not a consequence of nuclear pore transport defects (Figure S5D-E). We detected delayed import after Sec13 RNAi, as expected from previous studies (Figure S5F), and more efficient import in Ndc1-Sec13-expressing cells (Figure S5F). Nevertheless, we did not detect any defect in relocalization of heterochromatic DSBs after Kpt-276 or Importazol treatments, ruling out defective pore transport as a source of defective relocalization of heterochromatic DSBs (Figure S5G-H).

Together, we conclude that the nucleoplasmic fractions of Nup88, Nup98 and Sec13 are required for relocalizing heterochromatic DSBs to the nuclear periphery and repair progression, and that these functions are independent from their roles in nuclear pore transport.

Sec13 and Nup88 recruit Nup98 to DSBs downstream from Smc5/6

To better understand the interplay between Nup88, Nup98, and Sec13, we investigated the epistatic relationship between these components in DSB relocalization. RNAi depletion of Nup88+Sec13 results in a higher number of γH2Av foci in DAPI-bright 60 min after IR relative to individual RNAi depletions, indicating that these two proteins act independently in relocalizing heterochromatic DSBs (Figure 1B). Interestingly, Nup88+Nup98, Nup98+Sec13, and Nup88+Nup98+Sec13 RNAi lead to relocalization defects similar to Nup98 depletion alone (Figure 1C), consistent with Nup98 working with both Nup88 and Sec13 for relocalization. In addition, RNAi depletion of Nup88 or Sec13 significantly lowers the number of Nup98 foci colocalizing with γH2Av (Figure 1F), revealing a role for Nup88 and Sec13 in Nup98 loading to DSBs, similar to the role of Sec13 in Nup98 recruitment to transcription sites [20].

We further investigated the mechanisms responsible for Nup88-Nup98 and Sec13-Nup98 recruitment to repair sites. Previous studies showed that Nup98 recruitment to transcription sites requires the histone modifying complex MBD-R2 [39]. Human Nup98 also interacts with the DExH-Box Helicase 9 (Dhx9) [40], which contributes to HR repair [41, 42]. However, RNAi depletion of MBD-R2 or Dhx9 does not affect relocalization of heterochromatic DSBs, ruling out a role for these components in recruiting nucleoporins to repair sites for relocalization (Figure S2C-D).

We turned our attention to Smc5/6, which is required for relocalization of heterochromatic DSBs and acts downstream from silencing and resection [10, 12, 15]. RNAi depletion of Nup88+Nup98+Sec13+Smc5/6 results in similar relocalization defects as Nup88+Nup98+Sec13 RNAi (Figure 4A and Figure S6A), revealing that Nup88, Nup98 and Sec13 work in the same pathway as Smc5/6 for relocalization.

Subsequently, we investigated which steps of the Smc5/6-mediated relocalization pathway are dependent on Nup88, Nup98 and Sec13 by testing how depletion of these nucleoporins affects: damage signaling (*i.e.*, γH2Av-associated Mu2/Mdc1 or ATRIP foci [10]), Arp2/3 or myosin recruitment to repair sites [13], and Nse2 recruitment to heterochromatin and repair sites [10, 12]. Nucleoporin RNAi does not affect Mu2/Mdc1, ATRIP and Nse2 focus formation (Figure S6B), or Arp2/3, Myosin and Unc45 recruitment (Figure S6C). Consistent with normal Apr2/3 recruitment, nuclear actin filaments also form normally in the absence of nucleoporins (Figure S6D). However, RNAi depletion of Smc5/6 or SUMO E3-ligases affects Nup88, Nup98 and Sec13 enrichments at γH2Av foci (Figure 4B), placing nucleoporins recruitment downstream from Smc5/6 and SUMOylation.

In addition to mediating relocalization, Smc5/6 is required to exclude Rad51 foci from the heterochromatin domain [1, 10, 12]. Thus, we tested the role of nucleoporins in this function. Remarkably, Nup88, Nup98 or Sec13 RNAi results in abnormal formation of Rad51 foci inside the heterochromatin domain, and removal of Nup98 or all three nucleoporins results in a higher number of foci relative to Nup88 or sec13 RNAi depletions alone (Figure 4C and S6E,F). Additionally, RNAi depletion of Smc5/6 along with these nucleoporins results in a similar number of Rad51 foci inside the heterochromatin domain at 60 min post-IR to Smc5/6 RNAi alone (Figure 4D and Figure S6E,F), indicating that nucleoporins mediate Rad51 exclusion in the same pathway as Smc5/6.

Together, these results reveal that Sec13 and Nup88 independently recruit Nup98 to repair sites, and that these components act downstream of Smc5/6 for relocalization of heterochromatic DSBs and for Rad51 focus exclusion from the domain.

Nucleoporins are required for mobilizing and clustering heterochromatic DSBs.
The nucleoplasmic fractions of Nup88, Nup98 and Sec13 could promote relocalization of heterochromatic DSBs by either facilitating the mobilization of repair foci or by tethering repair sites to the nuclear periphery after relocalization, similar to the function of Nup107. We investigated this directly by characterizing the dynamics of repair sites using live imaging of Mu2/Mdc1 foci originating from the heterochromatin domain (marked by mCh-HP1a [10, 12, 13, 43]).

We previously showed that RNAi depletion of anchoring components at the nuclear periphery results in a higher plateau of the Mean Square Displacement (MSD) curve describing the dynamics of heterochromatic repair foci, consistent with increased exploration of the nuclear space [12]. In striking contrast, RNAi depletion of Nup88, Nup98 and Sec13 leads to a drastic reduction of the plateau of the MSD curve, reflecting decreased mobility (Figure 5A). Consistent with reduced dynamics, repair foci remain inside the heterochromatin domain throughout the 1h kinetic in the absence of Nup88, Nup98 and Sec13, while foci typically reach the nuclear periphery in control conditions during the same timeframe (Figure 5A). These results are consistent with a role for Nup88, Nup98 and Sec13 in mobilizing heterochromatic DSBs, rather than in anchoring repair sites to the nuclear periphery.

Next, we investigated which component of the movement is most affected in the absence of Nup88, Nup98 and Sec13 by quantifying the time points associated with directed or subdiffusive motion. We previously detected long directed motions (LDMs) associated with repair foci that

leave the heterochromatin domain, which typically occur in transit from the heterochromatin domain periphery to the nuclear periphery, *i.e.,* where most nuclear actin filaments are assembled (Figure 5B-C, S7A and [4, 13, 43]). Inside the heterochromatin domain foci move mostly by confined diffusive motion, in agreement with the existence of constraints on the movement and the lack of actin filaments [4, 13]. RNAi depletion of Nup88, Nup98 and Sec13 results in a significant reduction of LDM frequency and duration, consistent with most repair sites remaining inside the heterochromatin domain (Figure 5B-C and Figure S7A-B). However, the few repair sites that leave the domain still display directed motion, suggesting that LDMs are not primarily affected once repair foci are released from the heterochromatin domain (Figure 5B and Figure S7A-B). This is consistent with normal Arp2/3 and myosin recruitment to repair sites as well as normal actin filament formation after RNAi depletion of Nup88, Nup98 and Sec13 (Figure S6C-D).

Intriguingly, MSD analysis of the time points characterized by subdiffusive motion inside the heterochromatin domain also reveals a significant reduction in nuclear exploration during this initial phase of movement (Figure 5D) after RNAi depletion of Nup88, Nup98 and Sec13. This suggests that the primary consequence of losing Nup88, Nup98 and Sec13 is a reduced overall movement inside the heterochromatin domain, which in turn affects the ability of foci to reach the heterochromatin domain periphery and initiate directed motions. We also detected a reduced ability of repair foci to fuse and split inside the heterochromatin domain upon RNAi depletion of Nup88, Nup98 and Sec13, consistent with reduced dynamics (Figure 5E).

We conclude that Nup88, Nup98 and Sec13 nucleoporins mobilize repair sites inside the heterochromatin domain, promoting fusion and fission events and facilitating focus relocalization to the periphery of the heterochromatin domain independently from F-actin and myosins.

The phase separation properties of Nup98 are required and sufficient for relocalization of heterochromatic repair sites and Rad51 exclusion.

The Nup98FG construct, which is able to carry out relocalization of heterochromatic DSBs in the absence of endogenous Nup98 (Figure 3B), is largely composed of phenylalanine-glycine (FG) repeats (Figure S8A and [21]). These 'FG domains' are common components of nucleoporins that face the nuclear pore channel, where they create a phase separated environment via hydrophobic and aromatic (π-π) interactions between phenylalanine residues [44-47]. Consistently, Nup98 and the Nup98FG domain spontaneously phase separate *in vitro* at physiologic concentrations [47]. This property is highly conserved across species, including in *Drosophila* [47]. In agreement with their ability to phase separate, Nup98 FG domains mostly consist of intrinsically disordered regions (IDRs) (Figure S8A). Phase separation properties are also consistent with the importance of Nup98 in repair focus fusion and splitting behaviors (Figure 5E). Thus, we tested whether the phase separation properties of Nup98FG are required for relocalization of heterochromatic DSBs.

We generated mutant forms of Nup98FG that are either unable to phase separate (Nup98AG) or that restore hydrophobic interactions and phase separation properties (Nup98YG) by mutating all the FG repeats into AG or YG, respectively (Figure 6A-B) [44, 46]. We confirmed the effects of these mutations *in vivo* using an optoDroplet assay, where IDRs are fused to Cry2 to promote self-association upon blue light exposure (Figure S8B) [48]. When activated by light stimulation, Cry2-Nup98FG-mCherry and Cry2-Nup98YG-mCherry rapidly form droplets (Figure S8C-D and Movie S1), which undergo fusion and fission (Movie S2), confirming their phase separation properties. Furthermore, these droplets were quickly reversed upon light removal and could be re-induced by light exposure in the same cell multiple times (Figure S8E-F). Conversely, Cry2-Nup98AG-mCherry did not form droplets, similar to the negative control Cry2-mCherry, confirming its inability to phase separate (Figure S8C-D).

Next, we tested the effect of these mutations on relocalization of heterochromatic repair foci. Similar to Nup98FG, expression of Nup98YG in the absence of endogenous Nup98 results in normal relocalization of repair foci (Figure 6C and Figure S9A). Conversely, expression of the phase separation mutant Nup98AG results in heterochromatic breaks remaining inside the heterochromatin domain at 60 min and 4h after IR, consistent with a major relocalization defect (Figure 6C and Figure S9A). Notably, Nup98AG and Nup98YG are enriched at repair foci similarly to Nup98FG (Figure 6A-B), establishing that defective relocalization is not a consequence of defective recruitment of these proteins to damage sites.

A typical property of phase separated structures is selective permeability, *i.e.,* the ability to exclude certain proteins while enabling the passage of others. Thus, we tested the ability of Nup98-mediated phase separation to exclude Rad51 from repair foci inside the heterochromatin domain. Remarkably, expression of Nup98AG in the absence of endogenous Nup98 results in abnormal formation of Rad51 foci inside the heterochromatin domain (Figure 6D and Figure S9 B). Nup98YG expression restores Rad51 exclusion from the domain, similar to Nup98FG, revealing the importance of Nup98-mediated phase separation in Rad51 exclusion from repair sites inside the heterochromatin domain (Figure 6D and Figure S9B-C).

Relocalization of heterochromatic yH2Av foci and exclusion of Rad51 are also perturbed after cell treatment with 1,6-Hexanediol (Figure S9D-E), an aliphatic alcohol that weakens hydrophobic interactions and interferes with phase separation [46, 49], consistent with the importance of phase separation in these functions.

We next tested whether Nup98-dependent phase separation is sufficient to induce repair focus relocalization and Rad51 exclusion in heterochromatin by investigating whether artificially inducing phase separation is sufficient to rescue Nup98AG mutant defects. To achieve this, we used a dimerization system that fuses Nup98AG with an RGG domain that induces condensates, in the presence of the linker TMP-NVOC-Halo (TNH) [50, 51] (Figure 6E). Addition of TNH to the cell media results in the formation of Nup98AG condensates (Figure S9F). Strikingly, this is sufficient to restore normal relocalization of heterochromatic repair sites and Rad51 exclusion from the heterochromatin domain (Figure 6F-G and S9G-H).

Together, these studies revealed that the phase separation properties of Nup98 are required and sufficient to relocalize heterochromatic repair foci, and to block Rad51 recruitment inside the heterochromatin domain.

Nup98 phase separation properties are required for heterochromatin repair and stability.
These studies identified nucleoplasmic Nup88, Nup98 and Sec13 as new components required for relocalization of heterochromatic DSBs and for preventing Rad51 recruitment inside the heterochromatin domain, suggesting the importance of these proteins in the progression of heterochromatin repair. We directly tested this by determining the biological consequences of perturbing these nucleoporins and the phase separation properties of Nup98 on IR sensitivity, damage processing, and genome stability.

First, RNAi depletion of Nup88 and Sec13 (Figure S10A) or removal of the nucleoplasmic fraction of nucleoporins through Ndc1-tagging (Figure 7A) results in IR sensitivity, consistent with defective damage repair [12, 13]. Conversely, expression of the nucleoplasmic-only fraction of these nucleoporins (Nup88ΔC, Nup98FG, or Sec13 in a Nup96ΔN background, respectively) results in IR sensitivity comparable with controls expressing wild-type nucleoproteins (Figure 7A). Similarly, expression of Nup98AG mutants in the absence of endogenous Nup98 results in IR sensitivity, which is rescued by expression of Nup98YG (Figure 7B). This is in agreement with the importance of the nucleoplasmic fraction of Nup88, Nup98 and Sec13, and particularly the phase separation properties of Nup98, in IR resistance.

Second, RNAi depletion of Nup88, Nup98 or Sec13 results in persistent γH2Av foci associated with the heterochromatin domain 20h after IR in *Drosophila* cells (Figure 7C and Figure S10B), a time point at which heterochromatin repair is largely completed in control RNAi conditions (Figure 7C) [12, 13]. Stronger defects are observed after the simultaneous depletion of all three nucleoporins, consistent with Nup88 and Sec13 independently recruiting Nup98 for heterochromatin repair (Figure 7C). Similar persistent foci are detected when cells express the phase separation mutant construct Nup98AG, but not upon expression of Nup98YG, consistent with the importance of Nup98-driven phase separation in resolving heterochromatic DSBs (Figure 7D and Figure S10C).

Third, RNAi depletion of Nup88, Nup98 and Sec13 triggers the formation of damage-induced heterochromatic micronuclei, with the strongest phenotype observed after Nup88+Nup98+Sec13 RNAi (Figure 7E and Figure S10D). This is mimicked by the expression of Nup98AG and not by expression of Nup98YG, revealing the importance of Nup98-mediated phase separation in preventing micronucleus formation (Figure 7F and Figure S10E).

RNAi depletion or mutation of Nup88, Nup98 or Sec13 also results in genome instability in *Drosophila* larval neuroblasts (Figure 7G and Figure S10F-H), where abnormal karyotypes likely originate due to defective repair of spontaneous DSBs during larval development. Chromosome rearrangements include aneuploidies, chromosome fusions and changes in the number of satellites (Figure 7G and S10H), most of which involve the heterochromatic fourth and Y chromosomes or pericentromeric regions, as expected for defective heterochromatin repair (Figure S10H) [12, 13]. Together, we conclude that Nup88, Nup98 and Sec13 nucleoporins, and particularly the phase separation property of Nup98, are critical for heterochromatin repair and stability in *Drosophila* cells and tissues.

DISCUSSION

This study revealed a novel role for nucleoporins in heterochromatin repair and genome stability. Nup88 and Sec13 independently recruit Nup98 to heterochromatic DSBs downstream from Smc5/6, and these components are required to relocalize repair sites and to prevent Rad51 recruitment inside the heterochromatin domain. The nucleoplasmic function of these nucleoporins, and not their association with the nuclear periphery, is required for relocalization, revealing a novel 'off-pore' role for nucleoporins in DNA repair. Importantly, these nucleoporins mediate the mobilization of repair sites, promoting their clustering and subdiffusive motion at early relocalization steps. The phase separating properties of Nup98 are required and sufficient to promote this mobilization while also suppressing Rad51 recruitment, thus preventing aberrant recombination. Misregulation of this pathway results in heterochromatin repair defects and instability in cells and tissues. Together, these results support a model in which the nucleoplasmic fraction of Nup98 induces phase separation to create a selective barrier that blocks Rad51 access to heterochromatic repair foci, while promoting focus clustering and the diffusive motion of repair foci to the heterochromatin domain periphery. Once at the domain periphery, repair foci initiate directed motion to the nuclear periphery along actin filaments for HR repair progression (Figure 8).

How nucleoporins promote the mobilization of heterochromatic DSBs independently from nuclear F-actin and myosins is intriguing. Our study revealed that nucleoporins promote focus clustering and diffusion inside the heterochromatin domain, both of which are consistent with repair foci and heterochromatin behaving as phase separated structures. Remarkably, the condensation properties of Nup98 are required and sufficient for moving heterochromatic DSBs out of the heterochromatin domain. Thus, we propose that the initial mobilization of heterochromatic repair sites relies on the establishment of a multiphase condensate, with Nup98-dependent condensates forming inside the phase separated heterochromatin domain [52, 53]. The formation of a condensate inside another condensate, in conditions where the two

liquid phases are immiscible and have similar surface tension, results in capillary forces that push the smaller condensate to the surface of the larger one [54, 55]. These forces alone could explain how the establishment of Nup98-containing condensates promote relocalization of DSBs to the surface of the heterochromatin domain.

It is also noteworthy that artificially tethering an RGG domain to the Nup98AG phase separation mutant can rescue relocalization defects and the exclusion of Rad51 during the damage response. This suggests that the biophysical properties established by the RGG domain mimic some or all of the properties established by FG repeats during repair. Thus, the biophysical properties are likely more important than sequence composition of the seeding molecules for establishing the functions of Nup98 condensates in heterochromatin repair.

Collectively, our study suggests that Nup98-dependent phase separation contributes to heterochromatin repair at multiple levels (Figure 8): i) by promoting repair focus clustering, thus increasing the local concentration of repair components and early repair steps; ii) by facilitating the release of repair foci from the heterochromatin domain though capillary forces; and iii) by excluding Rad51 inside the heterochromatin domain by selective permeability, thus preventing aberrant recombination between repeated sequences.

The identification of Nup98 as a new DSB repair component working *via* the establishment of phase separated structures also raises new questions about how these structures interface with other condensates at repair sites, such as those formed by RPA [56], TopBP1 [57], Rad52 [58, 59], Slx4 [60], FUS [61, 62] and 53BP1 [63, 64]. Phase separated proteins can promote growth and changes in properties of pre-existing condensates through miscible properties [55], or maintain immiscible condensates with reduced protein exchanges [65], each specialized in a distinct repair step [65]. Consistent with this idea, it has been proposed that the interface between immiscible condensates allows for protein exchange, facilitating sequential biological reactions [65]. It is also tempting to speculate that the interaction between phase separated repair foci and nuclear F-actin affects nuclear dynamics [66]. For example, the wetting behavior of liquid condensates can facilitate their engagement with filamentous actin and movement along the filaments [55, 58, 66, 67]. Understanding the properties of and relationships between these structures is therefore an important future goal to better understanding the impact of condensates on repair progression and repair focus dynamics.

Intriguingly, our studies also identify the two functional modules of nucleoporins involved in heterochromatin repair: Nup88-Nup98 and Sec13-Nup98. These share a common structure including a β-propeller protein (Nup88 or Sec13) and an FG-containing protein (Nup98). β-propellers typically mediate protein-protein interactions, and in this context they appear to act as scaffolds for the recruitment of Nup98. Whether these interactions are direct is unclear, but a direct interaction between Nup98 and Nup88 has been previously described at the nuclear pore through the C-terminal domain of Nup98 [30]. This domain is not present in the Nup98FG construct we used, suggesting a different mode of interaction between Nup88 and Nup98 at DSBs. Interestingly, Alpha-fold modeling predicts that Nup98 can interact directly with Nup88 and Sec13 through loops protruding from the main barrel structure, and that this is dependent on the Nup98 Gle2-binding sequence (GLEBS) (Figure S11), which can similarly interact with the β-propeller Rae1 [68] (Figure S11). Thus, an interesting possibility is that Nup88 and Sec13 engage in direct interactions with the Nup98 GLEBS domain, and that these are distinct from interactions at the pore. Consistent with nucleoplasmic nucleoporins establishing different functional interactions at repair sites than those occurring at the pore, our studies also revealed that other FG-proteins interacting with Nup88 at the pore (Nup214 and Nup358) do not mediate relocalization of repair sites in heterochromatin.

Importantly, our studies suggest new mechanisms for nucleoporin-mediated oncogenic transformation. All Nup98-associated leukemias contain the Nup98FG domain fused with

transcription factors, chromatin modifiers, or other chromatin-associated proteins [27], and the oncogenic potential of Nup98 has been ascribed to its ability to form condensates [69-71]. The current model proposes that bringing the FG domain to transcription sites promotes myeloid transformation by altering gene expression [27, 71]. Our study suggests alternative mechanisms for oncogenic transformation: Nup98 oncofusions can titrate Nup98 away from repair sites or abnormally recruit transcriptional activators to heterochromatic repair sites, either of which would hijack the repair response in heterochromatin, inducing massive genomic instability. Similarly, higher levels of Nup88 have been linked to higher cancer aggressiveness [25, 26], which could also derive from misregulation of heterochromatin repair.

Together, these studies establish a new role for nucleoplasmic nucleoporins in nuclear dynamics, heterochromatin repair, and genome stability in multicellular eukaryotes, providing a new framework for understanding how their misregulation contributes to cancer initiation and progression.

FIGURE LEGENDS

Figure 1. Nup88, Nup98 and Sec13 nucleoporins are required for relocalization of heterochromatic DSBs. (A) Schematic representation of nuclear pore proteins including chromatin-associated nucleoporins. Red indicates nucleoporins whose depletion affects relocalization/anchoring of heterochromatic DSBs from this study or [12]. (B) Immunofluorescence (IF) (left) and quantification (right) of cells fixed 60 min after IR show the number of γH2Av foci in DAPI-bright and total foci following indicated RNAi depletions. *P<0.05, **P<0.01, ****P<0.0001, *n*> 195 cells for RNAi condition. (C) As described in B, except cells expressing MycFLAG-Nup96 were used. **P<0.01, ****P<0.0001, n> 328 cells for RNAi condition. (D) Wb shows the chromatin-bound fractions of Nup88, Nup98, and Sec13 at indicated time points after IR. Histone H4 is a loading control. (E) IF (top) and quantification (bottom) show the number of γH2Av foci colocalizing with the indicated nucleoporins in DAPI-bright, at different timepoints after IR. Dashed boxes and zoomed details highlight colocalizations. Nup98FG (see methods and Figure S4A,C) was used in place of Nup98 WT due to the stronger nucleoplasmic signal associated with this mutant. *n*>118 foci for each time point. (F) Quantification of cells fixed 10 min after IR shows the number of γH2Av foci colocalizing with Nup98FG foci in DAPI-bright following indicated RNAi depletions. ****P<0.0001 for the indicated comparisons and for all the comparison relative to Ctrl , *n*>74 foci for RNAi condition. Error bars: SEM in E, and SD in B,C,F from three or more independent experiments. P values calculated with two-tailed Mann–Whitney test. Images are max intensity projections of Z-stacks spanning the DAPI-bright region. Ctrl = Control. Scale bar = 1μm. See also Figures S1 and S2.

Figure 2. Constitutive anchoring of Nup88, Nup98, and Sec13 to the nuclear periphery results in defective relocalization. Schematic representations (top of each figure panel) show the experimental setup. (A) Cells expressing MycFLAG-Nup88-Ndc1 are treated with dsRNAs for Nup88 UTR to deplete endogenous Nup88, or a control (Ctrl). IF (left) and quantification (right) show the number of γH2Av foci in DAPI-bright at different timepoints after IR, following indicated RNAi depletions. *P<0.05, **P<0.01, *n*>27 cells for each time point. (B) As in (A), except cells express MycFLAG-Nup98-Ndc1 and RNAi depletion targets Nup98 UTR. ****P<0.0001, *n*>100 cells for each time point. (C) As in (A), except cells express MycFLAG-Sec13-Ndc1 and RNAi depletion targets Sec13 UTR. ****P<0.0001, *n*>100 cells for each time point. Error bars: SEM. P values calculated with two-tailed Mann–Whitney test. Images are max intensity projections of Z-stacks spanning the DAPI-bright region. Scale bar = 1μm. See also Figures S3.

Figure 3. Nucleoplasmic-only expression of Nup88, Nup98 or Sec13 results in normal relocalization. Schematic representations (top of each figure panel) show the experimental setup. (A) Cells expressing FHA-Nup88ΔC are treated with dsRNAi for Nup88 UTR to deplete endogenous Nup88, or a control (Ctrl). *n*>77 cells for each time point. (B) As in (A), except cells express FHA-Nup98FG and dsRNAs to target Nup98 UTR. *n*>100 cells for each time point. (C) As in (A), except cells express MycFLAG-Nup96ΔN and dsRNAs target only endogenous Nup96 (see also Fig. S4A, D-F). *n*>24 cells for each time point. Error bars: SEM. Images are max intensity projections of Z-stacks spanning the DAPI-bright region. Scale bar = 1μm. See also Figures S4.

Figure 4. Nup88, Nup98 and Sec13 are required for relocalization and to prevent abnormal Rad51 recruitment downstream from Smc5/6. (A) Quantification of cells expressing MycFLAG-Nup96 fixed 60 min after IR, shows the number of γH2Av foci in DAPI-bright after indicated RNAi depletions. ****P<0.0001 relative to Ctrl, n>226 cells for each condition. (B) Quantification of cells expressing MycFLAG-Nup88 (left), MycFLAG-Sec13 (middle), and GFP-Nup98FG (right) shows colocalizations with γH2Av foci 10 min after IR, following indicated RNAi depletions. ****P<0.0001 relative to Ctrl, *n*>495 foci for each condition. (C) Immunofluorescence (IF) and quantification of cells fixed 60 min after IR show the number of Rad51 foci in DAPI-bright and total foci following indicated RNAi depletions. Smc5/6 RNAi results in abnormal Rad51 focus formation in heterochromatin [10, 12, 15] and is used as positive control. *n*>246 cells for each condition. **P<0.01, ****P<0.0001 relative to Ctrl. (D) As in C. ****P<0.0001 for the indicated comparisons, n>581 cells for each RNAi condition. Error bars: SD from three or more experiments. P values calculated with two-tailed Mann–Whitney test. Scale bar = 1μm. See also Figures S6.

Figure 5. Nup88, Nup98, and Sec13 nucleoporins are required for the mobilization of heterochromatic DSBs. (A) 3D reconstructions in Imaris and MSD analysis of all heterochromatic GFP-Mu2 foci that form inside the mCh-HP1a domain after IR, following indicated RNAi depletions. *n* ≥ 46 tracks for each condition. Dashed boxes and zoomed details highlights the tracks. Δ*t*, time intervals (40s each). (B) LDM analysis of foci from the experiment described in (A). Duration and distribution of LDMs (black lines) along each track relative to different nuclear positions, adjusted relative to a 'pseudo-trajectory' defined by the average time that foci spend in each nuclear space and shown for equalized time intervals. *n*=53 foci for Ctrl and *n*=46 foci for Nup88+Nup98+Sec13 RNAi, from three experiments. Numbers on the left side indicate individual cells. (C) Average duration of directed and non-directed motions for heterochromatic foci in (A,B), in the indicated nuclear locations. ****P>0.0001 for the total average time in the nuclear location 1 for Nup88, Nup98, Sec13 RNAi relative to the Ctrl. (D) MSD analysis of time points from (A) characterized by non-directed motion inside the heterochromatin domain, following indicated RNAi depletions.****P>0.0001, *n*=29 foci for Ctrl and *n*=38 foci for Nup88+Nup98+Sec13 RNAi, from three experiments. Confinement radius (right) was calculated using the plateau of the curve (dashed line), as indicated in [43]. (E) IF (left) and quantification (right) show fusion and spitting events for heterochromatic Mu2/Mdc1 foci in cells expressing GFP-Mu2 and mCh-HP1a, following indicated RNAi depletions. Dashed box and zoomed detail highlights fusion-splitting events. In the box plot blue line is the mean; black line is the median *n*>97 foci per each condition. ***P<0.001 for the indicated comparison. Error bars are SEM in A, C, D. In E the whiskers are drawn down to the 10th percentile and up to the 90th. P values calculated with extra sum-of-squares *F*-test, nonlinear regression for curve fitting for A, D and two-tailed Mann–Whitney test in C, E. Scale bars, 1 µm. See also Figures S7.

Figure 6. Nup98 mediates relocalization of heterochromatic DSBs *via* phase separation. (A-B) (Top) Schematic representation of Nup98FG mutations. Each Phenylalanine of the FG-domain of Nup98FG is substituted with Alanine (blue) in Nup98AG or Tyrosine (green) in Nup98YG. (Bottom) IF shows Nup98AG and Nup98YG foci colocalizing with γH2Av foci.

Dashed box and zoomed details highlight colocalizations. (C) Quantification of γH2Av foci in DAPI-bright at different time points after IR, in cells expressing FHA-Nup98FG, FHA-Nup98AG or FHA-Nup98YG following RNAi depletion of endogenous of Nup98. ****P<0.0001 for Nup98AG relative to Nup98FG, n>35 cells for each time point. (D) Quantification of cells expressing FHA-Nup98FG, FHA-Nup98AG or FHA-Nup98YG following depletion of endogenous Nup98 (Nup98 UTR RNAi), fixed 60 min after IR, shows the number of Rad51 foci in DAPI-bright. ****P<0.0001 for indicated comparisons. n>363 cells for each RNAi condition. Smc5/6 RNAi in cells expressing Nup98FG is shown as a positive control. (E) Schematic representation of the dimerizer system (adapted from [50]). The RGG domain is tagged with mCherry (mCh) and fused to eDHFR, and Nup98AG is tagged with GFP and fused to three Haloenzymes. The dimerizer is TNH. (F) Quantification of cells expressing (+) or non-expressing (-) RGG-mCherry-RGG-eDHFR, plus Halo-GFP-Nup98AG, treated for 120 min with (+) or without (-) TNH, and fixed 60 min after IR, shows the number of γH2Av foci in DAPI-bright. ****P<0.0001. n>346 cells for each condition. (G) As in G, except Rad51 foci were stained and quantified. ****P<0.0001. n>342 cells for each condition. Error bars are SEM in C, and SD in D,F,G from three independent experiments. P values calculated with two-tailed Mann–Whitney test. Scale bars, 1 μm. See also Figures S9.

Figure 7. Nup88, Nup98, and Sec13 nucleoporins are required for heterochromatin repair and stability. (A) IR sensitivity assays show cell survival at different IR doses and after indicated RNAi depletions and protein expression. Rad51 RNAi results in cell sensitivity to IR [12, 13] and is used as positive control in cells expressing each FL (full-length) protein or Nup96ΔN, as indicated. First graph (left to right): Survival of cells expressing FHA-Nup88-Ndc1 or FHA-Nup88FL in the absence of endogenous Nup88 (Nup88 UTR RNAi). ****P<0.0001 for all comparisons *vs* Nup88FL. Second graph: Survival of cells expressing FHA-Sec13-Ndc1 or FHA-Sec13FL, after Sec13 UTR RNAi. ****P<0.0001 for all comparisons *vs* Sec13FL. Third graph: Survival of cells expressing FHA-Nup98FL, MycFLAG-Nup98-Ndc1, or FHA-Nup98FG, after Nup98 UTR RNAi. ****P<0.0001 for Nup98Ndc1 or Rad51 RNAi *vs* Nup98FL, P=ns for Nup98FG vs Ctrl. Fourth graph: Survival of cells expressing FHA-Nup88ΔC or FHA-Nup88FL, after Nup88 UTR RNAi. P=ns for Nup88ΔC vs Nup88FL. ****P<0.0001 for Rad51 *vs* FHA-Nup88FL or FHA-Nup88ΔC. Fifth graph: Survival of cells expressing MycFLAG-Nup96ΔN after RNAi depletion of: Ctrl; endogenous Nup96 (Nup96 UTR RNAi); Sec13+Nup96 (positive control); or Rad51+Nup96 (positive control). ****P<0.0001 for Sec13+Nup96 or Rad51+Nup96 *vs* Ctrl RNAi, P=ns for Nup96 vs Ctrl RNAi. n >150 cells per RNAi per dose. (B) IR sensitivity assay shows cell survival at different IR doses in cells expressing FHA-Nup98FG, FHA-Nup98AG or FHA-Nup98YG, following Nup98 UTR RNAi depletion. ****P<0.0001 for Nup98AG or Rad51 *vs* Nup98FG. n>100 cells per RNAi per dose. Rad51 RNAi is used as positive control in cells expressing Nup98FG. (C) IF (left) and quantification (right) of cells fixed 20 hrs after IR and stained for γH2Av and H3K9me2, following indicated RNAi depletions.****P<0.0001 for indicated comparisons, n>367 cells for each condition. +H3K9me2: γH2Av foci associated with H3K9me2 signals. (D) As in C, in cells expressing FHA-Nup98FG, FHA-Nup98AG or FHA-Nup98YG, following Nup98 UTR RNAi depletion. ****P<0.0001 for Nup98AG vs Nup98FG, n> 273 cells. (E) IF (left) and quantification (right) of micronuclei in cells stained for DNA (DAPI), heterochromatin (H3K9me2), and nuclear periphery (Nup62), after indicated RNAi depletions and IR treatment. **P<0.01 for indicated comparisons, n>447 cells for each RNAi condition. +/-H3K9me2: micronuclei with/without H3K9me2. Dashed box and zoomed details highlights a micronucleus. (F) As in E, in cells expressing FHA-Nup98FG, FHA-Nup98AG or FHA-Nup98YG , after Nup98 UTR RNAi depletion. ****P<0.0001 for Nup98AG relative to Nup98FG, n> 556 cells. (G) Image and quantification of karyotypes from Ctrl and indicated RNAi depleted or mutant larval brains stained by FISH for indicated satellites. Examples of fusions (arrowheads) and chromosome arm losses (dashed circle) are highlighted. Satellite positions are noted on the diagram of *Drosophila* chromosomes. n>46 karyotypes/genotype from at least two independent crosses and three brains. Nup98 RNAi lines also express Nup96-Myc (see

[24]. ****P<0.0001 for the indicated comparisons. The diagram of *Drosophila* chromosomes indicates satellite positions. Error bars are SEM in G and SD from three or more experiments in A-F. P values calculated with extra sum-of-squares *F*-test, nonlinear regression for curve fitting for A and B and two-tailed Mann–Whitney test in C-G. Images are max intensity projections of a few Z-stacks. Scale bar= 1μm. See also Figures S10.

Figure 8. Model for the role of Nup88, Nup98 and Sec13 in heterochromatic DSBs repair in *Drosophila*. DSBs are resected inside the heterochromatin domain, where Smc5/6 promotes the loading of Nup88-Nup98 and Nup98-Sec13. Nup98-FG repeats create a phase separated environment that facilitates focus clustering inside the heterochromatin domain and early steps of heterochromatin repair, while excluding Rad51. The multiphase condensate established by Nup98 inside the HP1a domain generates capillary forces that promote the relocalization of Nup98 condensates at repair sites to the surface of the heterochromatin domain. Here, Nup98-driven wetting behavior might also promote the association of repair foci with actin filaments generated by Arp2/3. Unc45 recruitment by Smc5/6 activates nuclear myosins to 'walk' repair sites along filaments, thus relocalizing DSBs to nuclear pores where HR continues with Rad51 recruitment. Relocalization prevents ectopic recombination by isolating damaged sites and their homologous templates (grey lines) from undamaged repeats before strand invasion.

Supplementary Figure Legends:

Supplementary Figure 1. Related to Figure 1. (A) Wb analyses show Sec13, Elys, and Nup98 RNAi depletion efficiencies. Lamin, Actin or (*) a non specific band, are used as loading controls. qPCR analyses show Nup62, Nup88 and Nup358 RNAi depletion efficiencies. GFP fluorescence intensity was used to monitor the RNAi efficiency in GFP-Nup98FG cells. ****P<0.0001, *n*>20 cells. P values calculated with two-tailed Mann–Whitney test. (B) Wb analysis (left) and IF (right) shows that Nup214 RNAi depletion affects Nup88 protein level. Wb analyses (bottom)show Nup214 depletion efficiency in cells expressing Nup88ΔC, where Nup88 stability is not affected. (C-D) Quantifications of cells fixed 60 min after IR show the number of γH2Av foci in DAPI-bright and total foci following indicated RNAi depletions, n>218 cells for each RNAi condition. (E) Images show that RNAi depletions of Nup88 or Sec13 do not affect Nup107 localization and have intact nuclear pores (MAb414 staining). (F) Images show that Nup98 RNAi depletion does not affect Nup153 localization. Given that loss of Nup107 from the nuclear periphery affects Nup153 localization [12], this also indicates normal Nup107 association with pores. (G) Wb shows the cytoplasmic fractions of Nup88, Nup98, and Sec13 at indicated time points after IR exposure. Histone H4 is a loading control. (H) Quantification of the experiment described in Figures 1E shows the total number of γH2Av foci colocalizing with with the indicated nucleoporins in DAPI-bright, at different timepoints after IR. Error bars are SEM in A, H and SD from three or more experiments in C-D. Images are max intensity projections. Scale bar= 1μm.

Supplementary Figure 2. Related to Figure 1. Nup88, Nup98 and Sec13 are required for relocalization of heterochromatic DSBs. (A) Quantification shows Nup88, Nup98 or Sec13 foci colocalizing with γH2Av foci 30 min after IR, following indicated RNAi depletions. ****P<0.0001, n>193 foci for MycFLAG-Nup88, n>75 foci for MycFLAG-Sec13 and n>208 foci for GFP-Nup98FG (B) Quantification of γH2Av foci colocalizing with H3K9me2 and Nup88, Nup98 or Sec13 at 10 min after IR. n>300 foci (C) qPCR analyses show Dhx9 and MBD-R2 RNAi depletion efficiencies. (D) Quantifications of cells fixed 60 min after IR show the number of γH2Av foci in DAPI-bright and total foci following indicated RNAi depletions. n>363 cells. ****P<0.0001 for the indicated comparison. Error bars are SEM in A, B, and SD from three experiments in D. P values calculated with two-tailed Mann–Whitney test.

Supplementary Figure 3. Related to figure 2. Constitutive anchoring of Nup88, Nup98, and Sec13 to the nuclear periphery results in defective relocalization. (A) Wb analysis shows depletion efficiencies for Nup88 in MycFLAG-Nup88-Ndc1 cells after Nup88 UTR RNAi, and for Sec13 in MycFLAG-Nup96ΔN cells following Nup96 RNAi. dsRNAs target the region deleted in Nup96ΔN, which is present in endogenous Nup96. (*) A non-specific band is used as loading control. (B-D) Quantifications of the experiment described in Figures 3A-C shows the total number of γH2Av foci at indicated timepoints after IR. (E-G) Schematic representations (top) show the experimental setup. Cells expressing wild type MycFLAG-Nup88 (E) Nup98 (F) or Sec13 (G), were treated with RNAi directed to the corresponding endogenous protein. Quantifications of cells fixed 60 min after IR show the number of γH2Av foci in DAPI-bright and the total number of foci. n>173 cells for each RNAi condtion. Error bars are SEM in B-D, and SD from three independent experiments in E-G.

Supplementary Figure 4. Related to Figure 3. Nucleoplasmic Nup88, Nup98 and Sec13 are required for relocalization. (A) Schematic representation of indicated WT and mutant proteins used in Figure 3. Numbers indicate aminoacid positions. (B) IF (left) shows Nup88 released from the nuclear periphery in cells expressing FHA-Nup88ΔC following Nup88 UTR RNAi. Quantification (right) of the experiment described in Figure 3A shows the total number of γH2Av foci. (C) IF (left) shows Nup98 is released from the nuclear periphery in cells expressing FHA-Nup98FG following Nup98 UTR RNAi. Quantification (right) of the experiment described in Figure 3B shows the total number of γH2Av foci. (D) Wb analysis shows Nup96 RNAi efficiency in FHA-Nup98FL, MycFLAG-Nup96ΔN-expressing cells following Nup96 RNAi depletion. (E) Schematic representation shows that Sec13 anchoring to the nuclear periphery is dependent on the N-terminal domain of Nup96, which complements the β-propeller of Sec13. Expression of a MycFLAG-Nup96ΔN mutant, while RNAi depleting endogenous Nup96, results in Sec13 release from the nuclear periphery. (F) IF (left) shows that Sec13 is released from the nuclear periphery in cells expressing MycFLAG-Nup96ΔN following endogenous Nup96 RNAi, while Nup107 is not affected. Quantification (right) of the experiment described in Figure 3C shows the total number of γH2Av foci. (G) IF shows Nup88ΔC (left) and Sec13 (right, in Nup96ΔN-expressing cells) foci colocalizing with γH2Av foci. Dashed boxes and zoomed details highlight colocalizations. Scale bars=1μm. Error bars are SEM in B,C,F.

Supplementary Figure 5. Related to Figures 1-3. Relocalization defects following nucleoporin RNAi or Ndc1 fusions is not a consequence of transport defects. (A) Scheme of the light-induced nuclear transport assay LEXY (adapted from [38]). (B) Representative images (top) and schematic representation (bottom) of the experiment with the LEXI probe to measure nuclear pore export/import. Upon blue-light exposure, the NLS-mCherry-LEXY probe translocates from the nucleus to the cytoplasm, allowing the measure of export. After blue-light exposure the probe returns to the nucleus, and import is measured by live imaging during a 30-min time interval as indicated. (C) Quantification of the nucleoplasmic/cytoplasmic ratio of fluorescence intensity over time for cells treated with the drugs Kp276 or Importazol (Ipz) (or DMSO control). ****P<0.0001.(D-F) Quantification of the nucleoplasmic/cytoplasmic ratio of fluorescence intensity over time for cells cells treated with the dsRNA targeting Nup88 (D, left), Nup98 (E, left), or Sec13 (F, left), or expressing MycFLAG-Nup88-Ndc1 (D, right), MycFLAG-Nup98-Ndc1 (E, right), MycFLAG-Sec13-Ndc1 (F, right). *P<0.05, **P<0.01, ****P<0.0001. n= 75 cells per each time point. (G-H) Quantifications show the number of γH2Av foci in DAPI-bright and total foci at indicated timepoints after IR, following indicated drug treatments. n>100 cells for each time point. Error bars are SEM in G,H, and SD from three experiments in C-F. P values calculated with two-tailed Mann–Whitney test.

Supplementary Figure 6. Related to Figure 4. Nup88, Nup98 and Sec13 are required for relocalization and to prevent abnormal Rad51 recruitment downstream from Smc5/6. (A) Quantification of the experiment described in Figure 4A shows the total number of γH2Av foci.

(B). Images (left) and quantifications (right) of indicated proteins in cells expressing GFP-Mu2, GFP-Atrip, or GFP-Nse2 plus mCherry(mCh)-HP1a (heterochromatin mark [10]). IF for Nse2 shows protein enrichments in heterochromatin before IR and focus formation 10 min after IR, following indicated RNAi depletions. n>655 foci for Mu2, n>297 foci for Atrip and n>155 foci for Nse2. In the box plot blue line:mean; black line:median (C) IF (top, example shown for Unc45) and quantification (bottom) of γH2Av foci colocalizing with FHA-Myo1A, Myo1B, MyoV, Arp3 or Unc45 10 min after IR, following indicated RNAi depletions. n>140 foci for each RNAi condition. (D) Quantification of dynamic nuclear actin filaments in response to IR in cells expressing the F-actin marker GFP-F-actCB-NLS, following indicated RNAi depletions, n>19 cells for each RNAi condition. (E) Quantification of foci after IF in undamaged cells (-IR) shows the number of Rad51 foci in DAPI-bright and total foci following indicated RNAi depletions. n>377 cells for each condition. (F) Quantification of the experiment described in Figure 4D shows the total number of Rad51 foci. Error bars are SEM in C, and SD in A, D, E, F from three experiments. In B the whiskers are drawn down to the 10th percentile and up to the 90th from three experiments.

Supplementary Figure 7. Related to Figure 5. (A) LDM analysis of foci from the experiment described in 5B. Duration and distribution of LDMs (blue lines) along each original track relative to different nuclear positions. (B) MSD analysis of time points corresponding to LDMs confirms that each identifies a directed motion.

Supplementary Figure 8. Related to Figure 6. (A) Analysis of *Drosophila* Nup98 protein using the Predictor of Natural Disordered Regions (PONDR) (http://www.pondr.com/ and [72]) shows the portions of the protein with higher predicted disorder. (B) Schematic representation of the constructs for the optoIDR assay (adapted from [48]). (C) Top: Schematic representation of the the optoIDR assay depicting clustering of Cry2-mCherry fusion proteins into optoDroplets upon blue light exposure. Bottom: representative images taken at indicated time points from blue light exposure for cells expressing indicated constructs. (D) Quantification of the experiment in (C). n>13 cells for each condition. ****P<0.0001 for Nup98FG vs Ctrl, **P<0.01 for Nup98YG vs Ctrl. Images (E) and quantification (F) show the reversibility and repeatable inducibility of Nup98FG optoDroplets by cycles of blue light activation for 4min followed by 30min recovery in the dark. n>42 cells. Scale bars=1μm. P values calculated with two-tailed Mann-Whitney test from three or more experiments.

Supplementary Figure 9. Related to Figure 6. Nup98 mediates relocalization of heterochromatic DSBs *via* phase separation. (A) Quantification of the experiment described in Figure 6C shows the total number of γH2Av foci. (B) Quantification of cells fixed 60 min after IR show the number of Rad51 foci in DAPI-bright and total foci in cells expressing FHA-Nup98FG, FHA-Nup98AG or FHA-Nup98YG, following Nup98 UTR RNAi depletion in undamaged conditions (-IR), *n*>471 cells for each condition. (C) Quantification of the experiment described in Figure 6D shows the total number of Rad51 foci. (D) Quantification of cells fixed 60 min after IR show the number of γH2Av foci in DAPI-bright and total foci following indicated 1.6 Hexanediol treatments *n*>150 cells for each condition. (E) Quantification of cells fixed 60 min after IR show the number of Rad51 foci in DAPI-bright and total foci following indicated 1.6-Hexanediol treatments *n*>462 cells for each condition. (F) Representative images from movies show Nup98AG condensates in cells expressing mCh-RGG-eDHFR and Halo-Nup98AG-GFP, after TNH addition to the media. (G) Quantification of the experiment described in Figure 6F shows the total number of γH2Av foci. (H) Quantification of the experiment described in Figure 6G shows the total number of Rad51 foci. Error bars are SEM in A and SD in B-E, G-H, from three experiments.

Supplementary Figure 10. Related to Figure 7. Nup88, Nup98 and Sec13 nucleoporins are required for heterochromatin repair and stability. (A) IR sensitivity assay shows cell survival

at different IR doses and after indicated RNAi depletions. ****P<0.0001 for all comparisons *vs* Ctrl. $n > 280$ cells per RNAi per dose. Rad51 RNAi is used as positive control. (B) Quantification of the experiment described in Figure 7C shows the number of persistent γH2Av foci not colocalizing with H3K9me2 signal (-H3K9me2). (C) Quantification of the experiment described in Figure 7D shows the number of γH2Av foci not associated with H3K9me2 signal (-H3K9me2). (D-E) Quantification of the experiment described in Figure 7E-F shows the number of micronuclei before IR. (F) Wb analysis (top) shows Nup98 depletion efficiency in Nup98 RNAi flies relative to ActinGal4/+ control (Ctrl). Lamin is a loading control. Wb analysis (middle) shows the loss of Sec13 in *sec13*^{01031} and *sec13*^{GS11919} mutant flies, relative to w^{1118} control (Ctrl). Tubulin is a loading control. qPCR analysis (bottom) shows Nup88 depletion efficiency in Nup88 RNAi flies relative to ActinGal4/+ control (Ctrl). (G) IF shows normal Nup107 and pore staining (Mab414) in salivary glands (top) and imaginal discs (bottom) of Nup98 RNAi flies expressing Nup96-Myc. (H) Images (left) of chromosome preparations from larval brains stained by FISH for AACAC, 359bp, and AATAT satellites and quantifications (right) show chromosome fusions and abnormalities in Sec13 mutants, Nup88 and Nup98 RNAi *vs* control flies. In Nup98 RNAi arrowhead highlights a chromosome fusion, asterisk highlights a chromosome fragment. In *Sec13*^{01031} arrowhead highlights translocation between X and 4th, dashed circle highlights a chromosome fusion plus arm loss. In *Sec13*^{GS11919} arrowheads highlight a fusion and arrow a filament connecting centromeres.Scale bar =1μm *P<0.05, **P<0.01, ***P<0.001, ****P<0.0001 for the indicated comparisons. P values calculated with two-tailed Mann–Whitney test with n>58 karyotypes/genotype from at least two independent crosses and three brains. Error bars are SEM in H and SD from three experiments in A-F. Images are max intensity projections of Z-stacks.

Supplementary Figure 11. Interaction models between the Nup98FG and Rae1, Sec13 or Nup88. Alphafold intersect models generated between Nup98FG and Rae1 (A), Sec13 (B), and Nup88ΔC (C), are shown. Blue: Nup98FG-GLEBS domain; Orange: aminoacids predicted to establish polar contacts. Purple: Rae1, Sec13 or Nup88ΔC as indicated.

METHODS

Cell culture

Kc167 (Kc) cells were used for all experiments and were maintained as logarithmically growing cultures in Schneider's medium (Sigma) + FBS (Gemini). Kc cells were authenticated by the *Drosophila* Genomic Resource Center (DGRC) and no mycoplasma contamination was detected.

Generation of cell lines expressing tagged proteins

Stable lines were obtained by cotransfecting the plasmid of interest with pCoHygro (Invitrogen) or pCoPuro (Addgene plasmid #17533) and selecting in the presence of 100 µg/ml Hygromycin B (Enzo Life Sciences) or 2 mg/ml Puromycin (Sigma-Aldrich). Transfections were performed with Cellfectin (Life Technologies), according to manufacturers' procedures.

IR Treatments

Cultures were exposed to IR using a 160 kV X-ray source (X-RAD iR-160, Precision X-Ray). We use a range of Gy at which the damage response (estimated based on the number of γH2Av foci) increases linearly with dose, and corresponds to nearly sublethal doses for controls (more than 90% survival at 2.5-10 Gy). A dose of 5 Gy was used for most experiments, unless otherwise indicated. The estimated number of DSBs induced by 5 Gy in *Drosophila* cells is approximately 7.5 DSBs in G1 and 14 DSBs in G2, which is based on published estimates of DSB numbers in mammalian cells, and the estimated genome size for human vs *Drosophila* cells. In kinetic analyses of fixed cells, time 0 (Unt) corresponds to cells fixed without exposure

to IR. In time-lapse experiments, time 0 (Unt) corresponds to cells imaged 5 min before IR treatment.

Plasmids

pCopia-mCherry-HP1a, pCopia-GFP-Mu2, pCopia-GFP-ATRIP, pCopia-GFP-Nse2 plasmids were previously described [10]. All other FHA-tagged or MycFLAG-tagged full-length (FL) proteins were generated by insertion of PCR-amplified sequences using the following cDNA from DGRC as templates: Nup88 (LD33348), Sec13 (LD03471), Ndc1 (LD42327), and Nup98-96 (RE74545). PCR products were cloned into AscI/PacI-digested pCopia-3XFLAG-StrepII-HA (FHA) vectors. FHA-Nup98FL was generated by PCR amplifying the Nup98 sequence of Nup98-96 fusion template. FHA-Nup98FG was generated by subcloning the Nup98FG sequence of DNA from DamNup98FG plasmid (kind gift from M. Fornerod) [21], into AscI/PacI-digested pCopia-3XFLAG-StrepII-HA vector. MycFLAG-Nup88-Ndc1 and MycFLAG-Sec13-Ndc1 plasmids were generated by subcloning the coding region of Ndc1 into KpnI/BspEI digested pCopia-MycFLAG-Nup88FL and pCopia-MycFLAG-Sec13FL vectors, respectively. pCopia-MycFLAG-Ndc1-Nup98 plasmid was generated by subcloning the MycFLAG-Ndc1 sequence from pCopia-MycFLAG-Ndc1-Sec13 plasmid into Eco47III/AscI-digested pCopia-Nup98FL vector. pCopia-MycFLAG-Nup96ΔN was generated by subcloning the PCR-amplified Nup96ΔN sequence into AscI/PacI-digested pCopia-MycFLAG-Nup96FL. pCopia-FHA-Nup88ΔC was generated by subcloning the PCR-amplified Nup88ΔC sequence into AscI/PacI-digested pCopia-MycFLAG-Nup88FL, and a SV40 NLS was inserted in C-terminus to compensate for the loss of a predicted NLS sequence in the Nup88ΔC mutant. pCopia-FHA-Nup98AG, pCopia-FHA-Nup98YG, pAWG-GFP-Nup98AG and pAWG-GFP-Nup98YG plasmids were generated by PCR amplification of Nup98AG and Nup98YG (obtained as geneblock from GENEWIZ) and cloning into AscI/PacI-digested pCopia-3XFLAG-StrepII-HA vector or pAWG-EGFP vector. NLS-mCherry-LEXY (pDN122) was from Barbara Di Ventura & Roland Eils (Addgene plasmid #72655). The LEXY construct was cloned out of pDN122 in which the NLS-mCherry-AsLOV2-NES21 domain was transformed into a pCopia promoter containing backbone and the NLS was swapped for a Drosophila NLS with optimized codons (KRKYF). Stable cells lines were made by introducing a Drosophila light-inducible nuclear export system (LEXY) construct into Kc or Kc cell lines expressing tagged nucleoporins of interest. pCRY2PHR-mCherryN1 was from Chandra Tucker (Addgene plasmid # 26866). Cry2PHR was cloned out of pmCherryN1 and transformed into a pCopia promoter containing backbone. pCopia-Flag-Cry2PHR-mCherry-Nup98FG/AG/YG plasmids were generated by subcloning the Nup98FG/AG/YG sequence from pCopia-FHA-Nup98FG/AG/YG plasmids into AscI/XhoI-digested pCopia-Flag-Cry2PHR. pHZ031-3xHalo-GFP-TRF1 and pHZ088-RGG-mCherry-RGG-eDHFR are plasmids gifted from Huaiying Zhang [51]. pCopia-RGG_mCherry_RGG_eDHFR was generated by PCR amplification of mCherry-RGG-eDHFR from pHZ088 and cloning into NheI-PacI-digested pCopia-3XFLAG-StrepII-HA vector. pCopia-3xHalo-GFP and pCopia-3xHalo-GFP-Nup98AG were generated by PCR amplification of 3xHalo-GFP from pHZ031 and cloning into AscI-NheI-digested pCopia-3XFLAG-StrepII-HA vector.

Fluorescence in Situ Hybridization (FISH)

Chromosome preparation and FISH protocols were previously described. AACAC, AATAT, and 359 bp probes were purchased from Integrated DNA Technologies. FISH probe sequences are listed in Table S1.

dsRNA synthesis and sequences

dsRNAs were prepared with the MEGAscript T7 Kit (Applied Biosystems). Amplicons for Bw, Smc5, Smc6, Rad51, Nse2/Cerv, and Nse2/ Qjt dsRNAs were previously described [10]. Amplicons used for all other dsRNAs were: Nup88 (DRSC16123), Sec13 (DRSC14114), Elys (DRSC31834/DRSC19571), Nup214 (DRSC04421/DRSC39709), Nup62 (DRSC06970/DRSC34583), Nup205 (DRSC19432/DRSC32817), Nup358 (DRSC34580/DRSC29772), MDB-R2 (DRSC37591/DRSC32494), Dhx9 (DRSC04921/DRSC37605), dPIAS (DRSC07721/

DRSC28335). Sequences can be found on the DRSC website (http://flyrnai.org). dsRNAs for Nup88UTR, Sec13UTR, Nup98UTR, Nup98 and Nup96 RNAi were prepared with the oligos listed in Table S1. When more than one amplicon is indicated, we combined equal amounts of each dsRNA for better efficiency of protein depletion.

RNAi depletions

dsRNAs were transfected with DOTAP Liposomal Transfection Reagent (Roche) following manufacturer's instructions. Incubation times and dsRNA amounts were optimized to maximize depletion efficiency while avoiding toxicity and cell cycle effects. For most RNAi depletions, cells were treated with dsRNAs for 5 days, except: Nup88 RNAi was done for 6 days; Nup98 RNAi was done for 3 days; RNAi depletion of endogenous Nup96 was done for 4 days. The control (Ctrl) used for all RNAi experiments is RNAi depletion of the *brown (bw)* gene. RNAi depletion efficiencies for *bw*, Smc5/6, Nse2/Cerv, Nse2/Qjt, dPIAS, Rad51, have been previously validated [10, 12, 13]. We note that all kinetics resulting from RNAi depletion must be compared to cells treated with control dsRNAs, since the γH2Av peak shifts from 10 min after IR in non-RNAi experiments to 30 min after IR in RNAi controls [10].

Antibodies

Antibodies used were: anti-Nup88 (1:1000 for IF, 1:10000 for Wb, kind gift from M. Hetzer); anti-Sec13 (1:1000 for IF, 1:200 for Wb, Capelson Lab); anti-Nup98 (1:1000 for IF, Capelson lab); anti-Nup62 (1:1000 for IF, Ohkura lab); anti-Nup107 (1:2000 for IF, kind gift from V. Doye), anti-FLAG (1:500 for IF, 1:1000 for Wb, Sigma); anti-HA (1:1000 for IF, Developmental Studies Hybridoma Bank); anti-GFP (1:500 for IF, Aves Lab); anti-H3K9me2 (1:500 for IF, Wako Chemicals); anti-H3K9me3 (1:500 for IF, Wako Chemicals); anti-H4 (1:1000 for Wb, Sigma); anti-Myc (1:1000 for IF, Developmental Studies Hybridoma Bank); anti-γH2Av (1:500 for IF, Rockland); anti-Rad51 (1:500 for IF, gift from J. Kadonaga); anti-Unc45 (1:500 for IF, gift from S. Bernstein); anti-Lamin/Dm0 (1:1000 for IF, 1:2000 for Wb, Developmental Studies Hybridoma Bank); anti-beta-actin (1: 2500 for Wb, Abcam); anti-alphatubulin (1:1000 for Wb, Sigma); anti-mab414 (1:1000 for IF, Biolegend). Secondary antibodies for immunofluorescence were from Life Technologies and Jackson Immunoresearch. Those used for western blotting were from Pierce and Santa Cruz Biotech. Antibodies were previously validated [10, 12, 13] or validated by comparing western blot or immunofluorescence signals in the presence of the protein of interest with signals after RNAi depletions, or immunofluorescence signals in the absence of primary antibodies.

qPCR

Total RNA was isolated from 3-5 x 10^6 cells or 5-10 larvae by Trizol extraction and treated with DNase I to remove any genomic DNA contaminant. RNA was used to generate single-stranded cDNA using random priming and Superscript Reverse Transcriptase III (Invitrogen). Specific transcripts were quantified using intron-spanning primers with iQ SYBR Green Supermix (Bio-Rad) and MyiQ Single Color, Real-Time PCR Detection System (Bio-Rad), according to manufacturer's instruction. Changes in transcript levels were normalized to Act5C mRNA for qPCR analysis of transcripts in cultured cells and to Lamin mRNA for qPCR analysis of transcripts in larvae. Each qPCR was repeated at least three times, and graphs show the average level of depletion relative to control RNAi. Oligonucleotides used for qPCR are listed in Table S1.

Western blotting

1–3×10^6 cells were collected, washed once in PBS and lysed for 15–20 min on ice with lysis buffer A (50 mM Tris, pH 7.8, 1% NP-40, 150 mM NaCl) containing protease inhibitors (Complete, Roche), 2-mercaptoethanol, and 1 mM PMSF. Benzonase was added to each sample. The soluble lysate was recovered by centrifugation (10 min, 4°C) and resuspended in the loading buffer (Laemmli 1x). Samples were denatured by 5 min incubation at 95°C before

running them on a TGX 4–12% or 10% gel (Bio-Rad) and transferred onto nitrocellulose membrane for hybridization with specific antibodies.

IR-sensitivity assay

IR sensitivity assay for RNAi depletion experiments was performed as previously described [13]. IR sensitivity assays for Ndc1-tagged Nup88 or Sec13 was performed as follows: dsRNAs for Nup88 or Sec13 UTRs were added on day 0 and 3, cells were irradiated on day 5, and quantified using trypan blue staining on day 8. IR sensitivity assays for Ndc1-Nup98 and Nup98FG were performed as follows: Rad51 dsRNAs were added on day 0, and Nup98UTR dsRNAs were added on day 2; cells were irradiated on day 5 and quantified on day 6. IR sensitivity assays for 'Nucleoplasmic only' Sec13 were performed as follows: Sec13UTR dsRNAs were added on day 0 and 3, Rad51 dsRNAs were added on day 1 and 3, endogenous Nup96 dsRNAs were added on day 2. Cells were irradiated on day 6, and quantified on day 8. IR sensitivity assays for Nup88ΔC were performed as follows: dsRNAs for endogenous Nup88 were added on day 0 and 4, Rad51 dsRNAs were added on day 1 and 4. Cells were irradiated on day 6, and quantified on day 9. IR sensitivity assays for the Nup98AG mutant were performed as follows: Nup98 UTR dsRNAs were added on day 0 and 3. Cells were irradiated on day 5, and quantified on day 6.

Quantification of Repair Foci in Fixed Samples

In IF experiments, classification of foci inside or outside the DAPI-bright region was done as previously described [10, 12]. Classification of foci inside and outside the heterochromatin domain was done by analyzing the position of foci relative to the H3K9me2 staining in each of the Z-stacks. Foci associated with the heterochromatin domain were either inside the H3K9me2 domain, at the periphery of the domain, or at the tips of H3K9me2 protrusions [10, 12].

Cell Imaging and Processing in Time-Lapse Experiments

Time-lapse experiments and quantification were performed as previously described [12, 13, 43]. For MSD analyses, cells were imaged with 40-sec time intervals for 60 min starting from 3-5 min after IR. 10 Z-stacks at 0.8 µm distance were imaged for 0.005 ms for GFP, and 0.015 ms for mCherry. The Coolsnap HQ2 camera was set at 2x2 binning for maximizing the intensity of the light collected and minimizing light exposure. All movies were corrected to compensate for modest photobleaching effects using softWorks (Applied Precision/GE Healthcare). For each nucleus, foci that appeared mostly 'static' were tracked with a semi-automated method in Imaris (Bitplane) and the "correct drift" function was applied to use these tracks for registering the nucleus. Foci were then tracked in 3D using an automated method and manually corrected to ensure optimal connections between timepoints. Focus positional data were extracted in Excel and analyzed in Matlab (MathWorks) and R using customized scripts [43]. MSDs were calculated as described in [43]. Positional data were also analysed using a customized script in R Studio to detect LDMs [43]. LDMs shown in Fig. 5B and Supplementary figure S7A correspond to the largest contiguous time interval containing MSDs of increasing slope for each focus. The ability of the script to correctly detect directed motions was confirmed by independent MSD analysis of the positional data within the time intervals of the LDMs, as shown in Supplementary figure 7B. For live imaging of nuclear actin filaments, a stable cell line expressing F-actCB–GFP–NLS was exposed to 5 Gy IR. The same field of cells was imaged before and every 5 min after IR for 60 min. Ten *z* stacks at 0.8 µm distance were imaged, starting 3–12 min after IR. 3D volume reconstructions and movie generation were done in Imaris (Bitplane). Quantification of filament length and angles of actin branches was done using the Measurement Tool in Imaris.

Chromatin fractionation

Fractionation of Kc cells was performed using the Thermo Scientific Subcellular Protein Fractionation kit for cultured cells (cat# 78840), following manufacturer's instructions. The cyto/

nucleoplasmic fractions and the chromatin fraction were subjected to Western blotting using indicated antibodies.

Dimerization assay

To recruit the arginine/glycine-rich (RGG) domain from the P granule component LAF-1 to Nup98AG, cells transfected with 3xHalo-GFP-Nup98AG (that has three Haloenzymes fused to Nup98AG) and RGG-mCherry-RGG-eDHFR plasmids were treated with the dimerizer TNH: TMP-NVOC-Halo [50, 51]. For live imaging, 1 μM TNH was added directly to cells in a chambered coverslip, between imaging timepoints. For IF, 1 μM TNH was added to the cell media and incubated for 2 h before fixing. Samples were covered and managed to minimize exposure of the dimerizer to light and heat before the experiments. Details of dimerizer synthesis and characterization with NMR spectra were previously described [50].

Light-induced nuclear pore transport assay

Nuclear transport assays were performed as described in the work of [38]. For blue light irradiation, the FITC channel was used (wavelengths/bandwidths: excitation 490/20 nm, emission 528/38 nm). Cells were imaged in the mCherry channel to establish initial nuclear signal intensity. Time-lapse microscopy was performed as previously described, and nuclear export of the LEXY construct was induced by applying a 1-s pulse of blue light from the FITC channel every 30 s for 15 min. Cells were then imaged every 5 min post nuclear export induction during a 30 min recovery period. Light intensity from the nucleus and cytoplasm of imaged cells was quantified in SoftWoRx or ImageJ and compared across timepoints. When indicated nuclear transport was inhibited by introducing 1 μM Kpt-276 or Importazol 40 min prior to imaging, to reduce nuclear export or import as in [73].

Cry2 optodroplet assay

Twenty-four hours prior to microscopy, cells were transfected with 2.5 ug plasmid DNA per well using DOTAP Liposomal Transfection Reagent (Roche) following manufacturer's instructions. Afterwards samples were loosely wrap in aluminum foil and placed in the tissue culture incubator. For optodroplet formation analyses, cells were exposed to 1s of blue light (488nm) every 25sec for 4 min, this ensured that the majority of the CRY2 population remained photoexcited during light treatment, with minimal toxicity. Cells where then imaged with 45-sec time intervals for 6 min starting from 15sec after blue light exposure. 10 Z-stacks at 0.8 μm distance were imaged for 0.015 ms for visualization of the mCherry signal. The Coolsnap HQ2 camera was set at 3x3 binning for maximizing the intensity of the light collected and minimizing light exposure. All movies were corrected to compensate for modest photobleaching effects using softWorks (Applied Precision/GE Healthcare). Acquisitions were done with the 60×objective. Cells with similar starting expression levels were compared for the formation of the optodroplets. For the determination of optodroplet stability, optodroplet formation was induced as described above for 4 minutes followed by mCherry detection without further blue light exposure for additional 30 min.

1,6 Hexanediol treatments

2.5, 5 or 7.5% 1,6-Hexanediol (Sigma-Aldrich, Cat number 240117) was added to the medium of *Drosophila* Kc cells starting from 10 min before 5 Gy IR exposure. Cells were fixed 1h after IR.

Micronucleus assay

For detecting micronuclei, Nup88 and Sec13 dsRNAs were added on day 0, and 5, and Nup98 dsRNAs were added on day 3 and 5. Cells were irradiated with 10 Gy on day 6, fixed on day 9 and processed for IF analysis. Micronuclei were detected as DAPI-positive signals outside the nuclear periphery.

Fly stocks and crosses
All crosses were carried out at 25°C, and flies were maintained as previously described [74]. Stocks were obtained from the Vienna *Drosophila* Resource Center (VDRC) (Nup88, w[1118] P{GD12047}v22446}), the Bloomington *Drosophila* Stock Center (BDSC) (Sec13, ry506 P{PZ} Sec13^{01031}/TM3, ryRK Sb1 Ser1), the Kyoto *Drosophila* Genetic Resource Center (DGRC) (Sec13, y1 w67c23; P{GSV6}GS11919/TM3, Sb1 Ser1). Nup98RNAi;Nup96 (w; UAS-Nup98/96RNAi-GD31198; UAS-Nup96-myc/TM6b) was a kind gift from M. Capelson [39]. w^{1118} was a kind gift from J. Tower. To obtain 3rd instar larvae for karyotyping of neuroblast metaphase spread, RNAi lines were crossed to the Act5c-GAL4 line (Bloomington #25374, rebalanced with a CyO, GFP balancer) and non-GFP larvae were picked for karyotyping as described [75].

Statistical analysis
All statistical analyses were performed using Prism6 (Graphpad Software).

Lead Contact and Materials availability
Further information and requests for resources and reagents should be directed to and will be fulfilled by the lead contact**,** Irene Chiolo (chiolo@usc.edu).

Data availability
Microscopy images are in the range of several Terabytes and would anyway require a trained eye for interpretation. They will hence be made available upon reasonable request.

Acknowledgments
This work was supported by AAUW International Fellowship to C.M.; USC Research Enhancement Fellowships to T.Ryu; USC Rose Hills Foundation Fellowship to N.B., NIH Training grant to C.S.; R01GM117376 and NSF Career 1751197 to I.C. We thank all the members of the Chiolo Lab for helpful discussions; M. Fornerod, M. Dasso, B. Di Ventura and R. Eils and H. Zhang for plasmids; Alexei Arnaoutouv from M. Dasso Lab for helpful advice; M. Hetzer, H. V. Doye, J. Kadonaga, H. Ohkura and S. Bernstein for antibodies; J. Tower for fly lines and media; BDSC (P40OD018537), VDRC, and DGRC (P40OD010949) for flies and plasmids. A. Christensen for input on the manuscript. A. Patel and L. Oei for generating constructs. G. Dialynas for help with larval tissue staining. L. Delabaere for Karyotyping training. Drosophila Rad51 antibodies are now maintained and distributed by the Chiolo Lab.

Declaration of Interests
The authors declare no competing interests.

References

1. Amaral, N., et al., Nuclear Dynamics of Heterochromatin Repair. Trends Genet, 2017. **33**(2): p. 86-100.
2. Caridi, P.C., et al., And yet, it moves: nuclear and chromatin dynamics of a heterochromatic double-strand break. Philos Trans R Soc Lond B Biol Sci, 2017. **372**(1731).
3. Caridi, C.P., et al., Nuclear actin filaments in DNA repair dynamics. Nat Cell Biol, 2019. **21**(9): p. 1068-1077.
4. Rawal, C.C., C.P. Caridi, and I. Chiolo, Actin' between phase separated domains for heterochromatin repair. DNA Repair, 2019. **81**: p. 102646.
5. Ho, J.W., et al., Comparative analysis of metazoan chromatin organization. Nature, 2014. **512**(7515): p. 449-52.
6. Smith, C.D., et al., The Release 5.1 Annotation of Drosophila melanogaster Heterochromatin, in Science. 2007. p. 1586-1591.
7. Hoskins, R.A., et al., The Release 6 reference sequence of the Drosophila melanogaster genome. Genome Res, 2015. **25**(3): p. 445-58.
8. Riddle, N.C., et al., Plasticity in patterns of histone modifications and chromosomal proteins in Drosophila heterochromatin. Genome Res, 2011. **21**(2): p. 147-63.
9. Peng, J.C. and G.H. Karpen, Epigenetic regulation of heterochromatic DNA stability. Curr Opin Genet Dev, 2008. **18**(2): p. 204-11.
10. Chiolo, I., et al., Double-strand breaks in heterochromatin move outside of a dynamic HP1a domain to complete recombinational repair. Cell, 2011. **144**(5): p. 732-44.
11. Li, Q., et al., The three-dimensional genome organization of Drosophila melanogaster through data integration. Genome Biol, 2017. **18**(1): p. 145.
12. Ryu, T., et al., Heterochromatic breaks move to the nuclear periphery to continue recombinational repair. Nat Cell Biol, 2015. **17**(11): p. 1401-11.
13. Caridi, C.P., et al., Nuclear F-actin and myosins drive relocalization of heterochromatic breaks. Nature, 2018. **559**(7712): p. 54-60.
14. Janssen, A., et al., A single double-strand break system reveals repair dynamics and mechanisms in heterochromatin and euchromatin. Genes Dev, 2016. **30**(14): p. 1645-57.
15. Ryu, T., M.R. Bonner, and I. Chiolo, Cervantes and Quijote protect heterochromatin from aberrant recombination and lead the way to the nuclear periphery. Nucleus, 2016. **7**(5): p. 485-497.
16. Dialynas, G., L. Delabaere, and I. Chiolo, Arp2/3 and Unc45 maintain heterochromatin stability in Drosophila polytene chromosomes. Exp Biol Med, 2019: p. 1535370219862282.
17. Jakob, B., et al., DNA double-strand breaks in heterochromatin elicit fast repair protein recruitment, histone H2AX phosphorylation and relocation to euchromatin. Nucleic Acids Res, 2011.
18. Chiolo, I., et al., Nuclear dynamics of radiation-induced foci in euchromatin and heterochromatin. Mutat Res, 2013. **750**(1-2): p. 56-66.
19. Tsouroula, K., et al., Temporal and Spatial Uncoupling of DNA Double Strand Break Repair Pathways within Mammalian Heterochromatin. Mol Cell, 2016. **63**(2): p. 293-305.
20. Capelson, M., et al., Chromatin-bound nuclear pore components regulate gene expression in higher eukaryotes. Cell, 2010. **140**(3): p. 372-83.

21. Kalverda, B., et al., Nucleoporins directly stimulate expression of developmental and cell-cycle genes inside the nucleoplasm. Cell, 2010. **140**(3): p. 360-71.
22. Vaquerizas, J.M., et al., Nuclear pore proteins nup153 and megator define transcriptionally active regions in the Drosophila genome. PLoS Genet, 2010. **6**(2): p. e1000846.
23. Liang, Y., et al., Dynamic association of NUP98 with the human genome. PLoS Genet, 2013. **9**(2): p. e1003308.
24. Pascual-Garcia, P. and M. Capelson, Nuclear pores as versatile platforms for gene regulation. Curr Opin Genet Dev, 2014. **25**: p. 110-7.
25. Martinez, N., et al., The nuclear pore complex protein Nup88 is overexpressed in tumor cells. Cancer Res, 1999. **59**(21): p. 5408-11.
26. Agudo, D., et al., Nup88 mRNA overexpression is associated with high aggressiveness of breast cancer. Int J Cancer, 2004. **109**(5): p. 717-20.
27. Michmerhuizen, N.L., J.M. Klco, and C.G. Mullighan, Mechanistic insights and potential therapeutic approaches for NUP98-rearranged hematologic malignancies. Blood, 2020. **136**(20): p. 2275-2289.
28. Kuhn, T.M., et al., Chromatin targeting of nuclear pore proteins induces chromatin decondensation. J Cell Biol, 2019. **218**(9): p. 2945-2961.
29. Fornerod, M., et al., The human homologue of yeast CRM1 is in a dynamic subcomplex with CAN/Nup214 and a novel nuclear pore component Nup88. EMBO J, 1997. **16**(4): p. 807-16.
30. Griffis, E.R., S. Xu, and M.A. Powers, Nup98 localizes to both nuclear and cytoplasmic sides of the nuclear pore and binds to two distinct nucleoporin subcomplexes. Mol Biol Cell, 2003. **14**(2): p. 600-10.
31. Roth, P., et al., The Drosophila nucleoporin DNup88 localizes DNup214 and CRM1 on the nuclear envelope and attenuates NES-mediated nuclear export. J Cell Biol, 2003. **163**(4): p. 701-6.
32. Bernad, R., et al., Nup358/RanBP2 attaches to the nuclear pore complex via association with Nup88 and Nup214/CAN and plays a supporting role in CRM1-mediated nuclear protein export. Mol Cell Biol, 2004. **24**(6): p. 2373-84.
33. Rosenblum, J.S. and G. Blobel, Autoproteolysis in nucleoporin biogenesis. Proc Natl Acad Sci U S A, 1999. **96**(20): p. 11370-5.
34. Stavru, F., et al., NDC1: a crucial membrane-integral nucleoporin of metazoan nuclear pore complexes. J Cell Biol, 2006. **173**(4): p. 509-19.
35. Enninga, J., A. Levay, and B.M. Fontoura, Sec13 shuttles between the nucleus and the cytoplasm and stably interacts with Nup96 at the nuclear pore complex. Mol Cell Biol, 2003. **23**(20): p. 7271-84.
36. Bonnin, E., et al., Biallelic mutations in nucleoporin NUP88 cause lethal fetal akinesia deformation sequence. PLoS Genet, 2018. **14**(12): p. e1007845.
37. Griffis, E.R., et al., Nup98 is a mobile nucleoporin with transcription-dependent dynamics. Mol Biol Cell, 2002. **13**(4): p. 1282-97.
38. Niopek, D., et al., Optogenetic control of nuclear protein export. Nat Commun, 2016. **7**: p. 10624.

39. Pascual-Garcia, P., J. Jeong, and M. Capelson, Nucleoporin Nup98 Associates with Trx/MLL and NSL Histone-Modifying Complexes and Regulates Hox Gene Expression. Cell Rep, 2014. **9**(5): p. 1981.
40. Capitanio, J.S., B. Montpetit, and R.W. Wozniak, Human Nup98 regulates the localization and activity of DExH/D-box helicase DHX9. Elife, 2017. **6**.
41. Chakraborty, P. and K. Hiom, DHX9-dependent recruitment of BRCA1 to RNA promotes DNA end resection in homologous recombination. Nat Commun, 2021. **12**(1): p. 4126.
42. Liu, M.Y., et al., ATR phosphorylates DHX9 at serine 321 to suppress R-loop accumulation upon genotoxic stress. Nucleic Acids Res, 2023.
43. Caridi, C.P., et al., Quantitative Methods to Investigate the 4D Dynamics of Heterochromatic Repair Sites in Drosophila Cells. Methods Enzymol, 2018. **601**: p. 359-389.
44. Frey, S., R.P. Richter, and D. Gorlich, FG-rich repeats of nuclear pore proteins form a three-dimensional meshwork with hydrogel-like properties. Science, 2006. **314**(5800): p. 815-7.
45. Frey, S. and D. Gorlich, A saturated FG-repeat hydrogel can reproduce the permeability properties of nuclear pore complexes. Cell, 2007. **130**(3): p. 512-23.
46. Patel, S.S., et al., Natively unfolded nucleoporins gate protein diffusion across the nuclear pore complex. Cell, 2007. **129**(1): p. 83-96.
47. Schmidt, H.B. and D. Gorlich, Nup98 FG domains from diverse species spontaneously phase-separate into particles with nuclear pore-like permselectivity. Elife, 2015. **4**.
48. Shin, Y., et al., Spatiotemporal Control of Intracellular Phase Transitions Using Light-Activated optoDroplets. Cell, 2017. **168**(1-2): p. 159-171 e14.
49. Ribbeck, K. and D. Gorlich, The permeability barrier of nuclear pore complexes appears to operate via hydrophobic exclusion. EMBO J, 2002. **21**(11): p. 2664-71.
50. Zhang, H., et al., Optogenetic control of kinetochore function. Nat Chem Biol, 2017. **13**(10): p. 1096-1101.
51. Zhang, H., et al., Nuclear body phase separation drives telomere clustering in ALT cancer cells. Mol Biol Cell, 2020. **31**(18): p. 2048-2056.
52. Larson, A.G., et al., Liquid droplet formation by HP1alpha suggests a role for phase separation in heterochromatin. Nature, 2017. **547**(7662): p. 236-240.
53. Strom, A.R., et al., Phase separation drives heterochromatin domain formation. Nature, 2017. **547**(7662): p. 241-245.
54. Shin, Y. and C.P. Brangwynne, Liquid phase condensation in cell physiology and disease. Science, 2017. **357**(6357): p. 1-11.
55. Gouveia, B., et al., Capillary forces generated by biomolecular condensates. Nature, 2022. **609**(7926): p. 255-264.
56. Spegg, V., et al., Phase separation properties of RPA combine high-affinity ssDNA binding with dynamic condensate functions at telomeres. Nat Struct Mol Biol, 2023. **30**(4): p. 451-462.
57. Frattini, C., et al., TopBP1 assembles nuclear condensates to switch on ATR signaling. Mol Cell, 2021. **81**(6): p. 1231-1245.e8.
58. Oshidari, R., et al., DNA repair by Rad52 liquid droplets. Nature Communications, 2020. **11**(1): p. 695.

59. Mine-Hattab, J., et al., Single molecule microscopy reveals key physical features of repair foci in living cells. Elife, 2021. **10**.
60. Alghoul, E., et al., Compartmentalization of the SUMO/RNF4 pathway by SLX4 drives DNA repair. Mol Cell, 2023. **83**(10): p. 1640-1658 e9.
61. Altmeyer, M., et al., Liquid demixing of intrinsically disordered proteins is seeded by poly(ADP-ribose). Nat Commun, 2015. **6**: p. 8088.
62. Singatulina, A.S., et al., PARP-1 Activation Directs FUS to DNA Damage Sites to Form PARG-Reversible Compartments Enriched in Damaged DNA. Cell Rep, 2019. **27**(6): p. 1809-1821 e5.
63. Kilic, S., et al., Phase separation of 53BP1 determines liquid-like behavior of DNA repair compartments. EMBO J, 2019. **38**(16): p. e101379.
64. Pessina, F., et al., Functional transcription promoters at DNA double-strand breaks mediate RNA-driven phase separation of damage-response factors. Nat Cell Biol, 2019. **21**(10): p. 1286-1299.
65. Mine-Hattab, J., S. Liu, and A. Taddei, Repair Foci as Liquid Phase Separation: Evidence and Limitations. Genes (Basel), 2022. **13**(10).
66. Miné-Hattab, J. and I. Chiolo, Complex Chromatin Motions for DNA Repair. Frontiers in Genetics, 2020. **11**(800).
67. Merigliano, C. and I. Chiolo, Multi-scale dynamics of heterochromatin repair. Curr Opin Genet Dev, 2021. **71**: p. 206-215.
68. Ren, Y., et al., Structural and functional analysis of the interaction between the nucleoporin Nup98 and the mRNA export factor Rae1. Proc Natl Acad Sci U S A, 2010. **107**(23): p. 10406-11.
69. Terlecki-Zaniewicz, S., et al., Biomolecular condensation of NUP98 fusion proteins drives leukemogenic gene expression. Nat Struct Mol Biol, 2021. **28**(2): p. 190-201.
70. Chandra, B., et al., Phase Separation Mediates NUP98 Fusion Oncoprotein Leukemic Transformation. Cancer Discov, 2022. **12**(4): p. 1152-1169.
71. Oka, M., et al., Phase-separated nuclear bodies of nucleoporin fusions promote condensation of MLL1/CRM1 and rearrangement of 3D genome structure. Cell Rep, 2023. **42**(8): p. 112884.
72. Peng, K., et al., Length-dependent prediction of protein intrinsic disorder. BMC Bioinformatics, 2006. **7**: p. 208.
73. Zhang, K., et al., The C9orf72 repeat expansion disrupts nucleocytoplasmic transport. Nature, 2015. **525**(7567): p. 56-61.
74. Ren, C., et al., Increased internal and external bacterial load during Drosophila aging without life-span trade-off. Cell Metab, 2007. **6**(2): p. 144-52.
75. Larracuente, A.M. and P.M. Ferree, Simple method for fluorescence DNA in situ hybridization to squashed chromosomes. J Vis Exp, 2015(95): p. 52288.

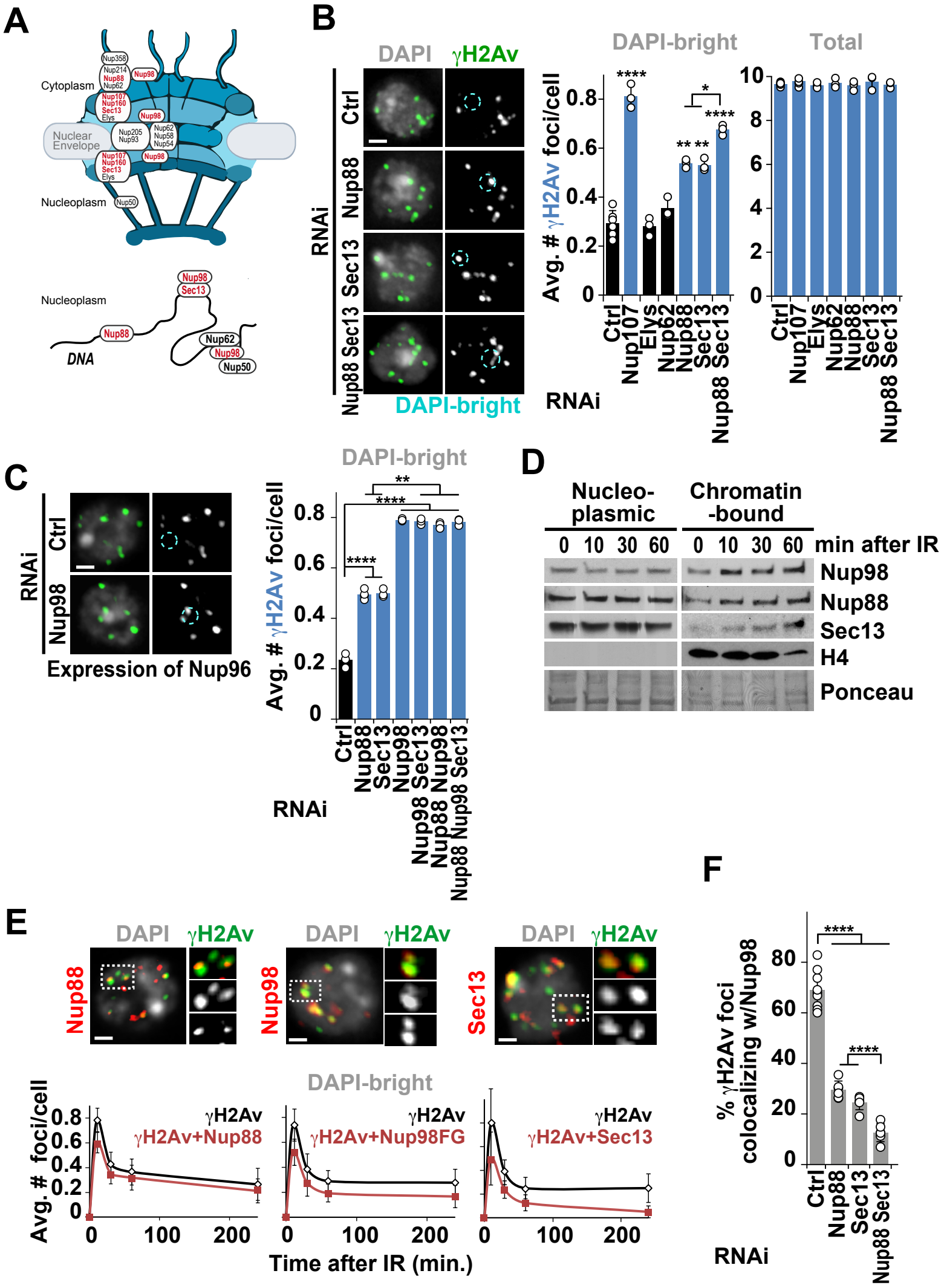
A
Cytoplasm
Nuclear Envelope
Nucleoplasm
Nup358
Nup214
Nup88
Nup62
Nup98
Nup107
Nup160
Sec13
Elys
Nup205
Nup93
Nup62
Nup58
Nup54
Nup50
Nucleoplasm
DNA
B
DAPI
γH2Av
RNAi
Ctrl
Nup88
Sec13
Nup88 Sec13
DAPI-bright
DAPI-bright
Total
Avg. # γH2Av foci/cell
Ctrl
Nup107
Elys
Nup62
Nup88
Sec13
Nup88 Sec13
RNAi
C
RNAi
Ctrl
Nup98
Expression of Nup96
DAPI-bright
Avg. # γH2Av foci/cell
Ctrl
Nup88
Sec13
Nup98
Nup98 Sec13
Nup88 Nup98
Nup88 Nup98 Sec13
RNAi
D
Nucleo-plasmic
Chromatin -bound
0 10 30 60
0 10 30 60
min after IR
Nup98
Nup88
Sec13
H4
Ponceau
E
DAPI
γH2Av
Nup88
Nup98
Sec13
DAPI-bright
Avg. # foci/cell
γH2Av
γH2Av+Nup88
γH2Av+Nup98FG
γH2Av+Sec13
Time after IR (min.)
F
% γH2Av foci colocalizing w/Nup98
Ctrl
Nup88
Sec13
Nup88 Sec13
RNAi

Figure 1

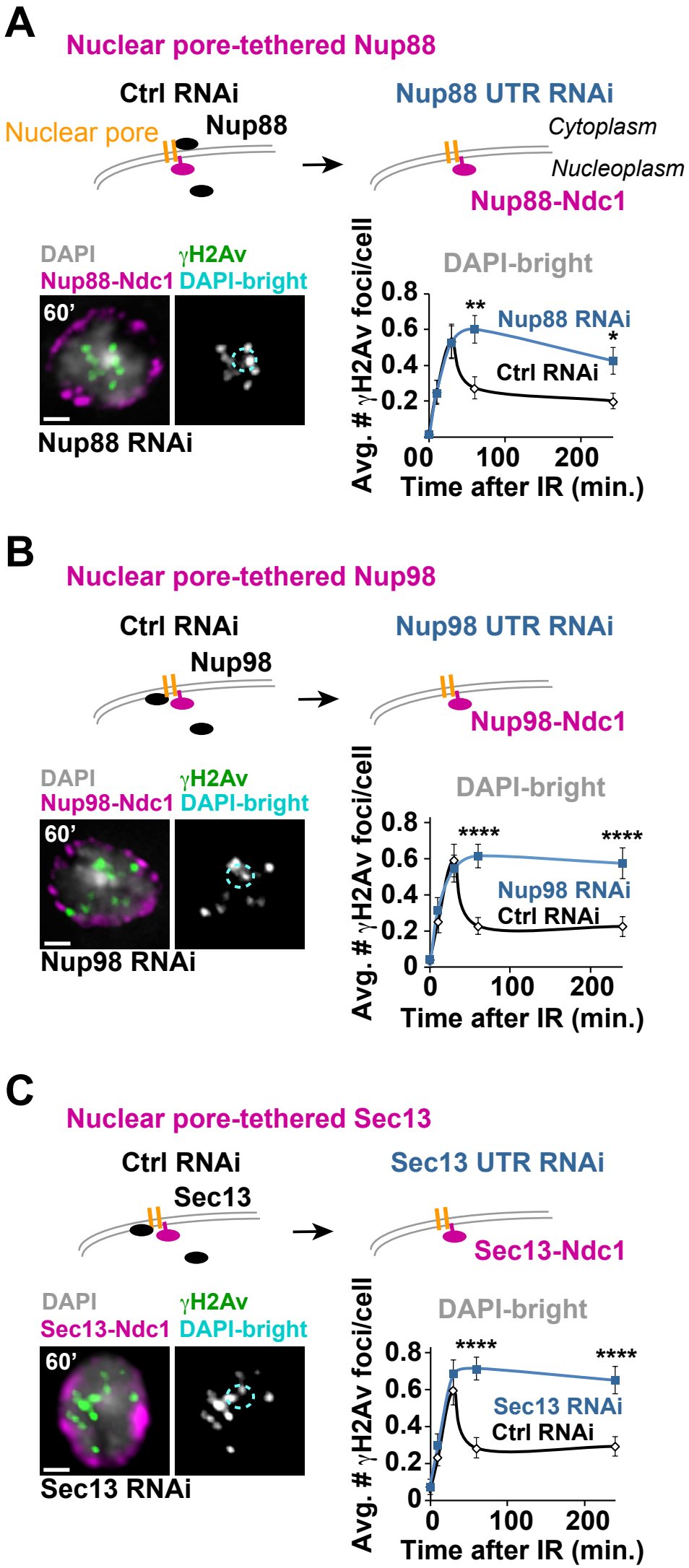
A
Nuclear pore-tethered Nup88
Ctrl RNAi
Nup88 UTR RNAi
Nuclear pore
Nup88
Cytoplasm
Nucleoplasm
Nup88-Ndc1
DAPI
γH2Av
Nup88-Ndc1
DAPI-bright
60'
Nup88 RNAi
DAPI-bright
Nup88 RNAi
Ctrl RNAi
Avg. # γH2Av foci/cell
Time after IR (min.)
B
Nuclear pore-tethered Nup98
Ctrl RNAi
Nup98 UTR RNAi
Nup98
Nup98-Ndc1
DAPI
γH2Av
Nup98-Ndc1
DAPI-bright
60'
Nup98 RNAi
DAPI-bright
Nup98 RNAi
Ctrl RNAi
Avg. # γH2Av foci/cell
Time after IR (min.)
C
Nuclear pore-tethered Sec13
Ctrl RNAi
Sec13 UTR RNAi
Sec13
Sec13-Ndc1
DAPI
γH2Av
Sec13-Ndc1
DAPI-bright
60'
Sec13 RNAi
DAPI-bright
Sec13 RNAi
Ctrl RNAi
Avg. # γH2Av foci/cell
Time after IR (min.)

Figure 2

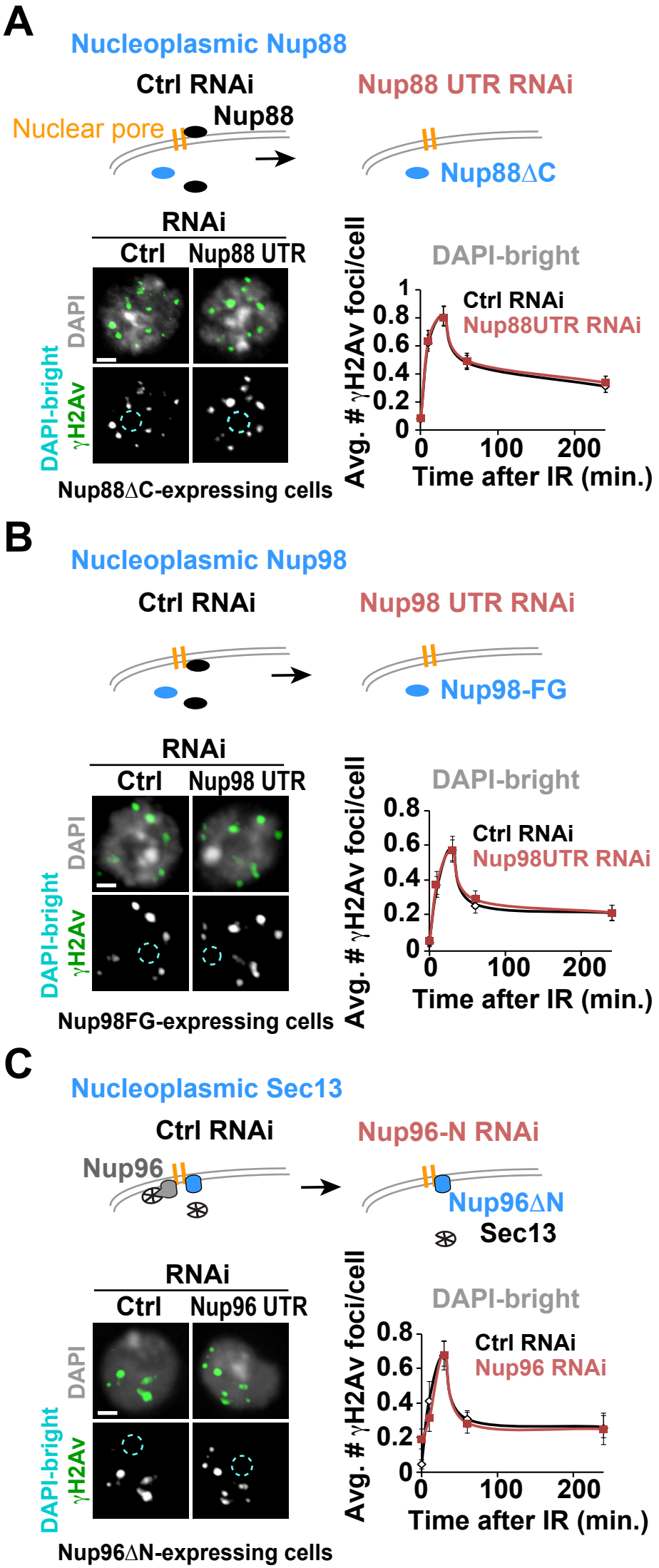
A
Nucleoplasmic Nup88
Ctrl RNAi
Nup88 UTR RNAi
Nuclear pore
Nup88
Nup88ΔC
RNAi
Ctrl
Nup88 UTR
DAPI
DAPI-bright
γH2Av
Nup88ΔC-expressing cells
DAPI-bright
Ctrl RNAi
Nup88UTR RNAi
Avg. # γH2Av foci/cell
Time after IR (min.)
B
Nucleoplasmic Nup98
Ctrl RNAi
Nup98 UTR RNAi
Nup98-FG
RNAi
Ctrl
Nup98 UTR
Nup98FG-expressing cells
DAPI-bright
Ctrl RNAi
Nup98UTR RNAi
Avg. # γH2Av foci/cell
Time after IR (min.)
C
Nucleoplasmic Sec13
Ctrl RNAi
Nup96-N RNAi
Nup96
Nup96ΔN
Sec13
RNAi
Ctrl
Nup96 UTR
Nup96ΔN-expressing cells
DAPI-bright
Ctrl RNAi
Nup96 RNAi
Avg. # γH2Av foci/cell
Time after IR (min.)

Figure 3

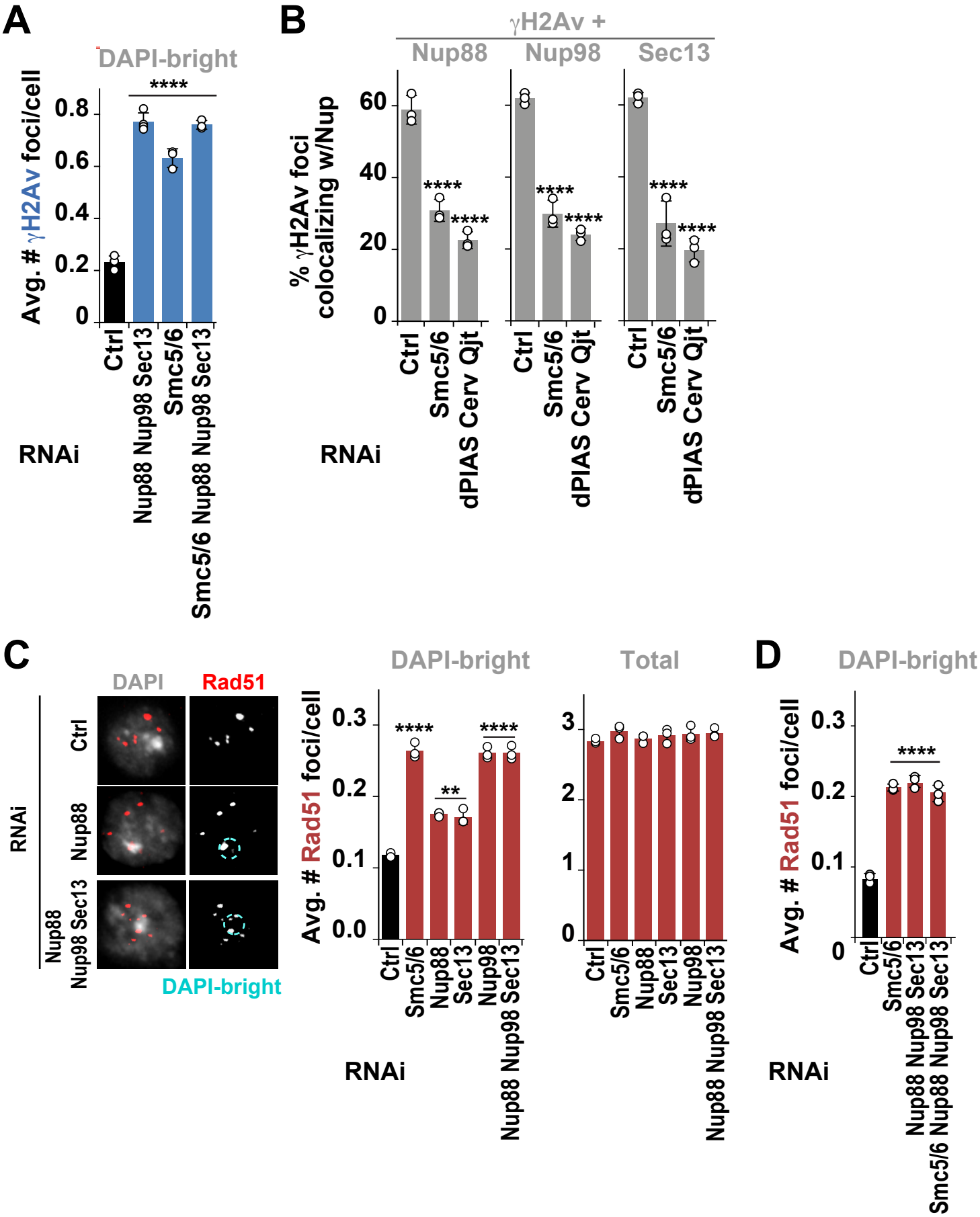
A
DAPI-bright
Avg. # γH2Av foci/cell
0
0.2
0.4
0.6
0.8
****
Ctrl
Nup88 Nup98 Sec13
Smc5/6
Smc5/6 Nup88 Nup98 Sec13
RNAi
B
γH2Av +
Nup88
Nup98
Sec13
% γH2Av foci colocalizing w/Nup
0
20
40
60
****
Ctrl
Smc5/6
dPIAS Cerv Qjt
RNAi
C
DAPI
Rad51
DAPI-bright
RNAi
Ctrl
Nup88
Nup88 Nup98 Sec13
Avg. # Rad51 foci/cell
0.0
0.1
0.2
0.3
**
Ctrl
Smc5/6
Nup88
Sec13
Nup98
Nup88 Nup98 Sec13
Total
0
1
2
3
D
DAPI-bright
Avg. # Rad51 foci/cell
0
0.1
0.2
0.3
Ctrl
Smc5/6
Nup88 Nup98 Sec13
Smc5/6 Nup88 Nup98 Sec13
RNAi

Figure 4

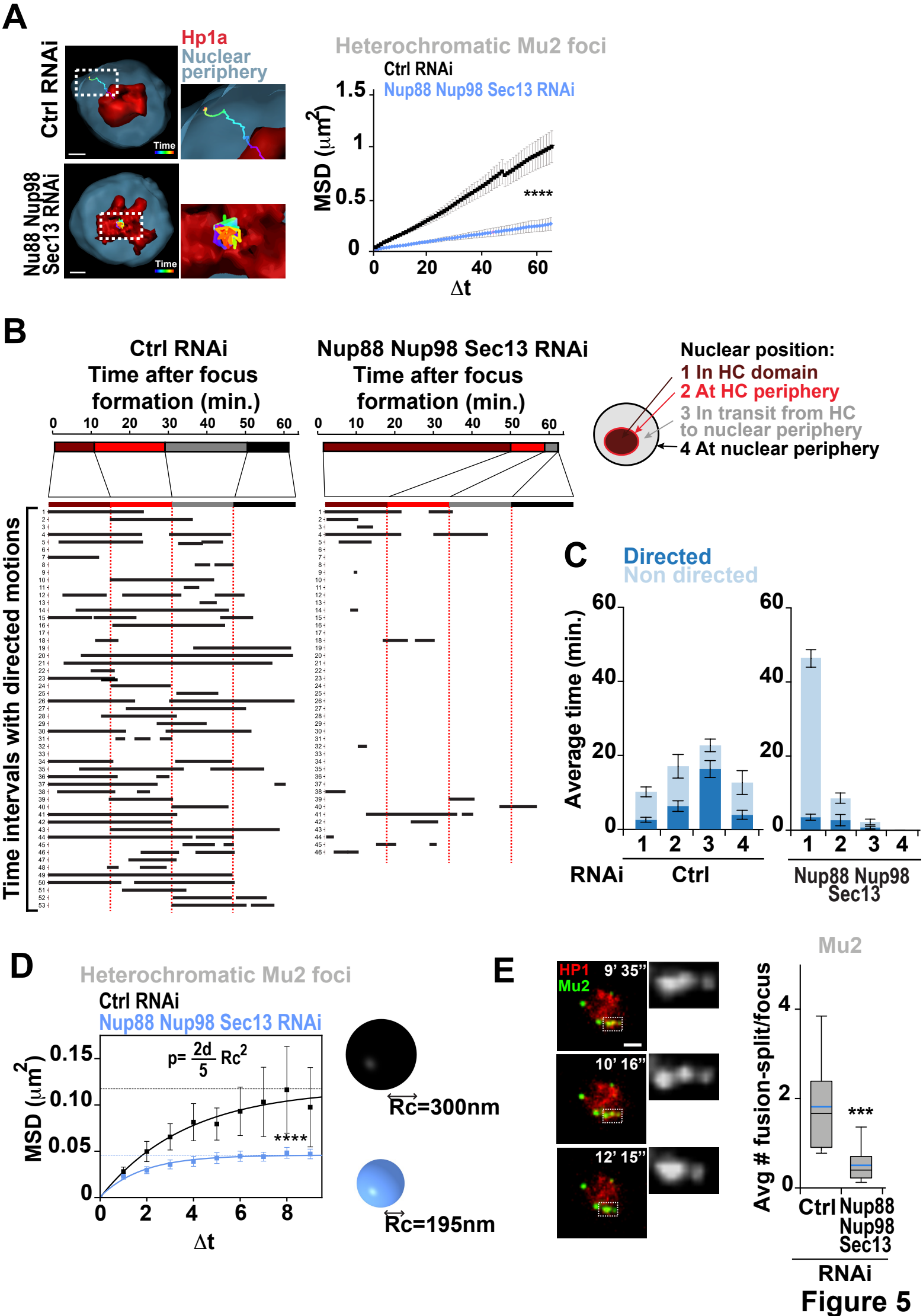
A
Hp1a
Nuclear periphery
Ctrl RNAi
Nu88 Nup98 Sec13 RNAi
Time
Heterochromatic Mu2 foci
Ctrl RNAi
Nup88 Nup98 Sec13 RNAi
MSD (μm²)
****
Δt
B
Ctrl RNAi
Time after focus formation (min.)
Nup88 Nup98 Sec13 RNAi
Time after focus formation (min.)
Time intervals with directed motions
Nuclear position:
1 In HC domain
2 At HC periphery
3 In transit from HC to nuclear periphery
4 At nuclear periphery
C
Directed
Non directed
Average time (min.)
RNAi
Ctrl
Nup88 Nup98 Sec13
D
Heterochromatic Mu2 foci
Ctrl RNAi
Nup88 Nup98 Sec13 RNAi
MSD (μm²)
p= 2d/5 Rc²
****
Δt
Rc=300nm
Rc=195nm
E
HP1
Mu2
9' 35"
10' 16"
12' 15"
Mu2
Avg # fusion-split/focus
***
Ctrl
Nup88 Nup98 Sec13
RNAi

Figure 5

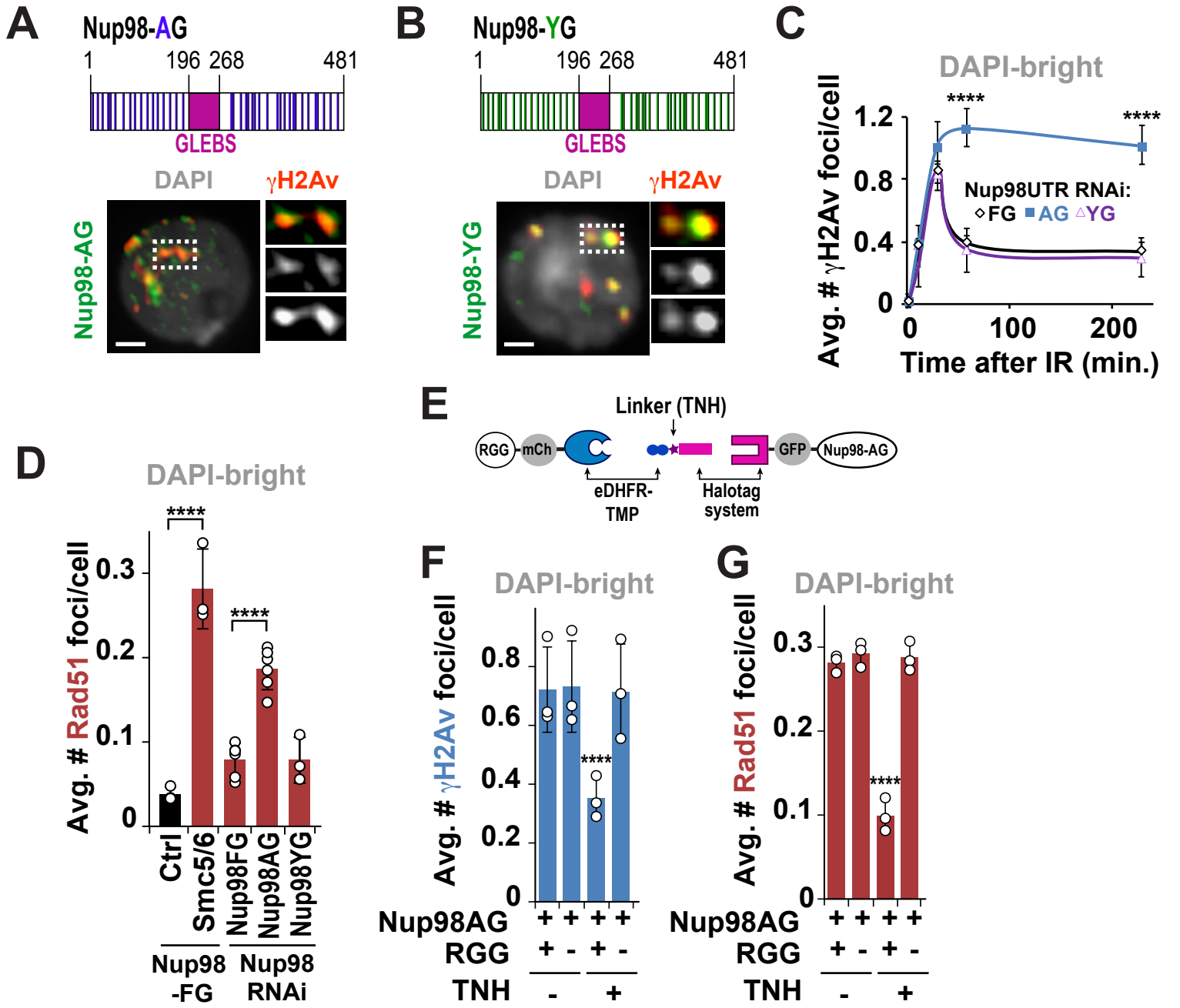
A
Nup98-AG
1
196 268
481
GLEBS
DAPI
γH2Av
Nup98-AG
B
Nup98-YG
1
196 268
481
GLEBS
DAPI
γH2Av
Nup98-YG
C
DAPI-bright
Avg. # γH2Av foci/cell
1.2
0.8
0.4
0
****
****
Nup98UTR RNAi:
FG AG YG
0
100
200
Time after IR (min.)
E
Linker (TNH)
RGG
mCh
GFP
Nup98-AG
eDHFR-TMP
Halotag system
D
DAPI-bright
Avg. # Rad51 foci/cell
0.3
0.2
0.1
0
****
****
Ctrl
Smc5/6
Nup98FG
Nup98AG
Nup98YG
Nup98 -FG
Nup98 RNAi
F
DAPI-bright
Avg. # γH2Av foci/cell
0.8
0.6
0.4
0.2
0
****
Nup98AG + + + +
RGG + - + -
TNH - +
G
DAPI-bright
Avg. # Rad51 foci/cell
0.3
0.2
0.1
0
****
Nup98AG + + + +
RGG + - + -
TNH - +

Figure 6

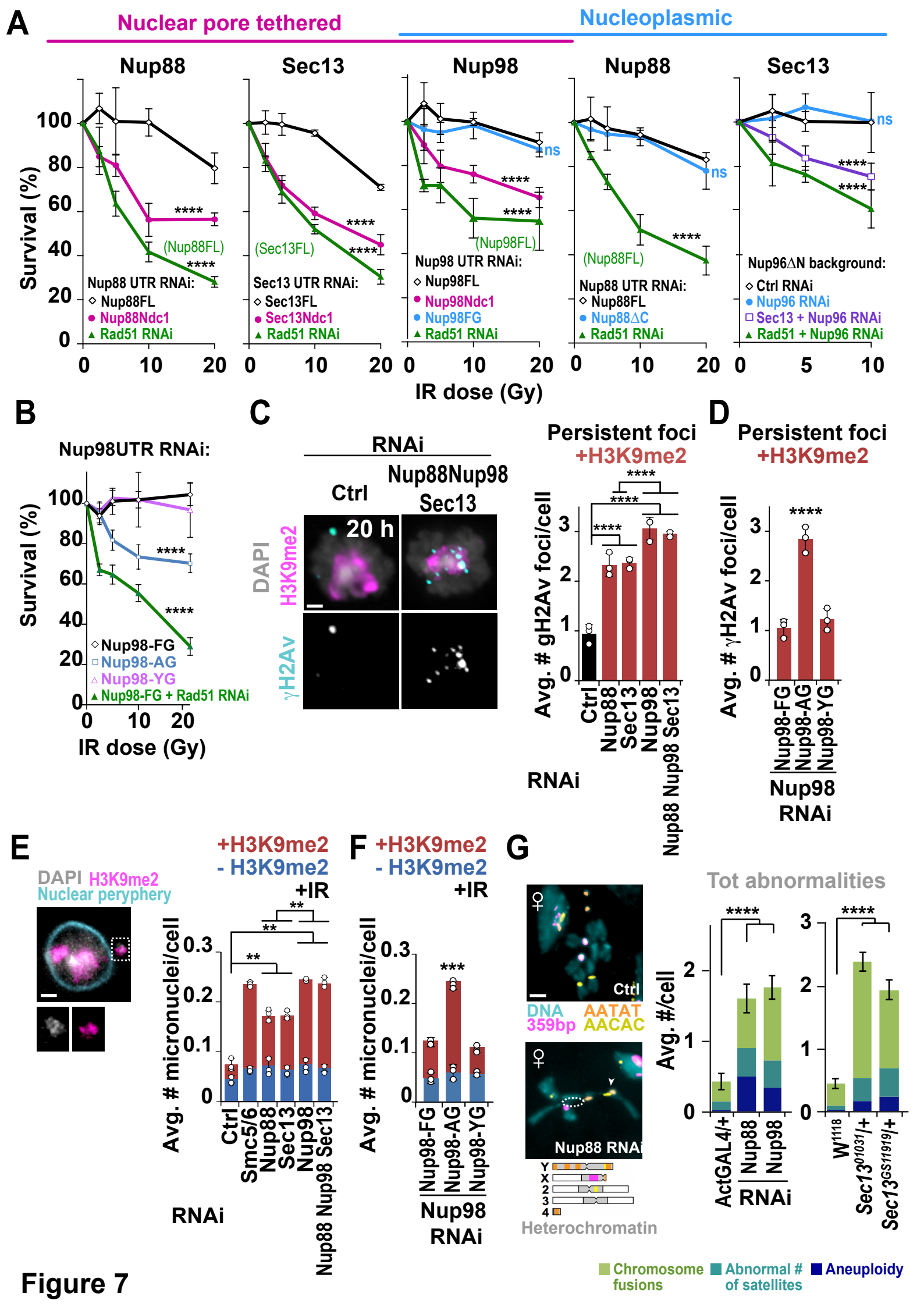
A
Nuclear pore tethered
Nucleoplasmic
Nup88
Sec13
Nup98
Nup88
Sec13
Survival (%)
IR dose (Gy)
Nup88 UTR RNAi:
Nup88FL
Nup88Ndc1
Rad51 RNAi
Sec13 UTR RNAi:
Sec13FL
Sec13Ndc1
Rad51 RNAi
Nup98 UTR RNAi:
Nup98FL
Nup98Ndc1
Nup98FG
Rad51 RNAi
Nup88 UTR RNAi:
Nup88FL
Nup88ΔC
Rad51 RNAi
Nup96ΔN background:
Ctrl RNAi
Nup96 RNAi
Sec13 + Nup96 RNAi
Rad51 + Nup96 RNAi
(Nup88FL)
(Sec13FL)
(Nup98FL)
(Nup88FL)
ns
****
B
Nup98UTR RNAi:
Survival (%)
IR dose (Gy)
Nup98-FG
Nup98-AG
Nup98-YG
Nup98-FG + Rad51 RNAi
C
RNAi
Ctrl
Nup88Nup98
Sec13
20 h
DAPI
H3K9me2
γH2Av
Persistent foci
+H3K9me2
Avg. # gH2Av foci/cell
Ctrl
Nup88
Sec13
Nup98
Nup88 Nup98 Sec13
RNAi
D
Persistent foci
+H3K9me2
Avg. # γH2Av foci/cell
Nup98-FG
Nup98-AG
Nup98-YG
Nup98 RNAi
E
DAPI H3K9me2
Nuclear peryphery
+H3K9me2
- H3K9me2
+IR
Avg. # micronuclei/cell
Ctrl
Smc5/6
Nup88
Sec13
Nup98
Nup88 Nup98 Sec13
RNAi
F
+H3K9me2
- H3K9me2
+IR
Avg. # micronuclei/cell
Nup98-FG
Nup98-AG
Nup98-YG
Nup98 RNAi
G
Ctrl
DNA
359bp
AATAT
AACAC
Nup88 RNAi
Y
X
2
3
4
Heterochromatin
Tot abnormalities
Avg. #/cell
ActGAL4/+
Nup88
Nup98
RNAi
W1118
Sec13 01031/+
Sec13 GS11919/+
Chromosome fusions
Abnormal # of satellites
Aneuploidy

Figure 7

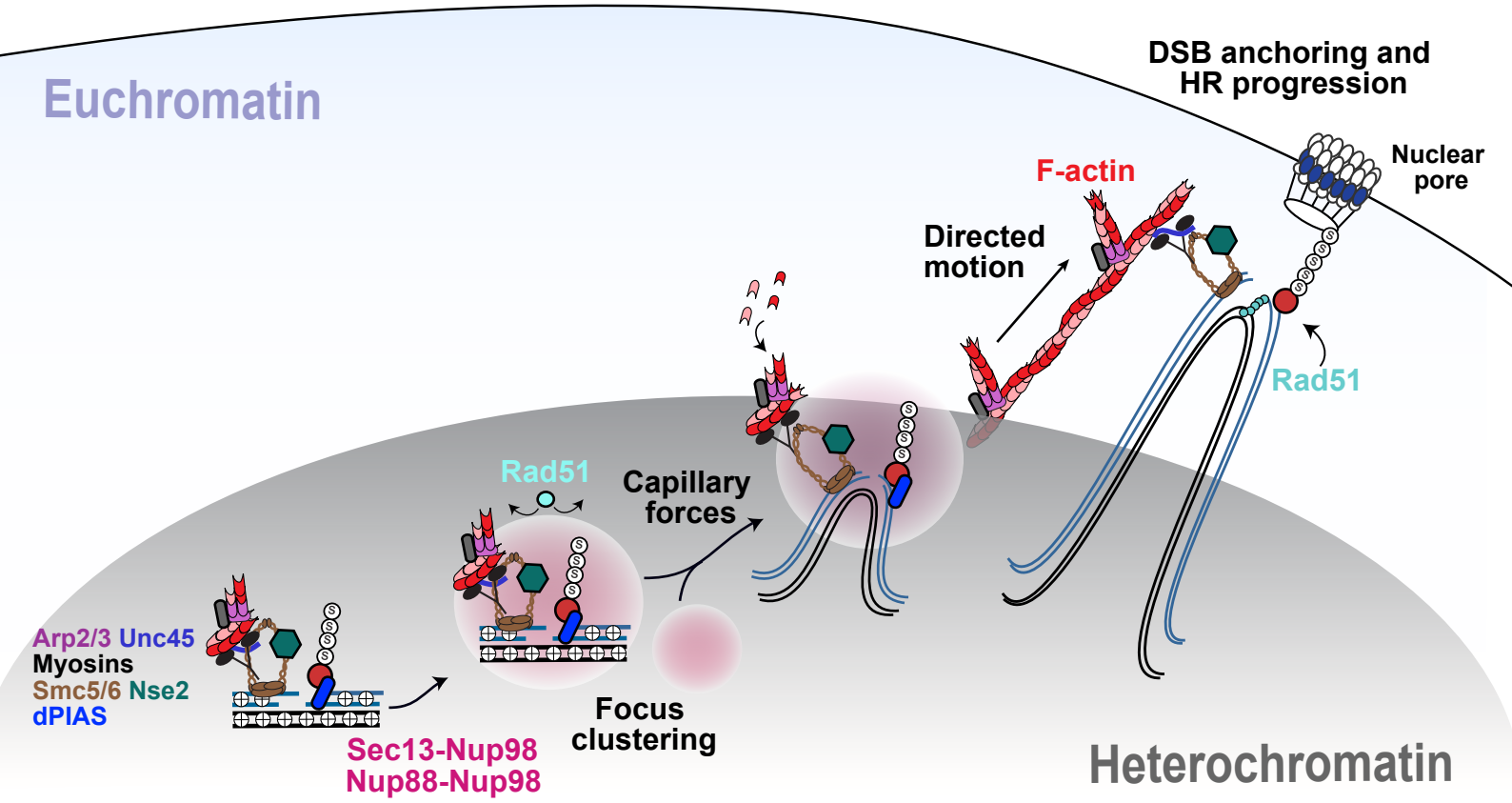
Euchromatin
DSB anchoring and
HR progression
Nuclear
pore
F-actin
Directed
motion
Rad51
Rad51
Capillary
forces
Arp2/3 Unc45
Myosins
Smc5/6 Nse2
dPIAS
Sec13-Nup98
Nup88-Nup98
Focus
clustering
Heterochromatin

Figure 8

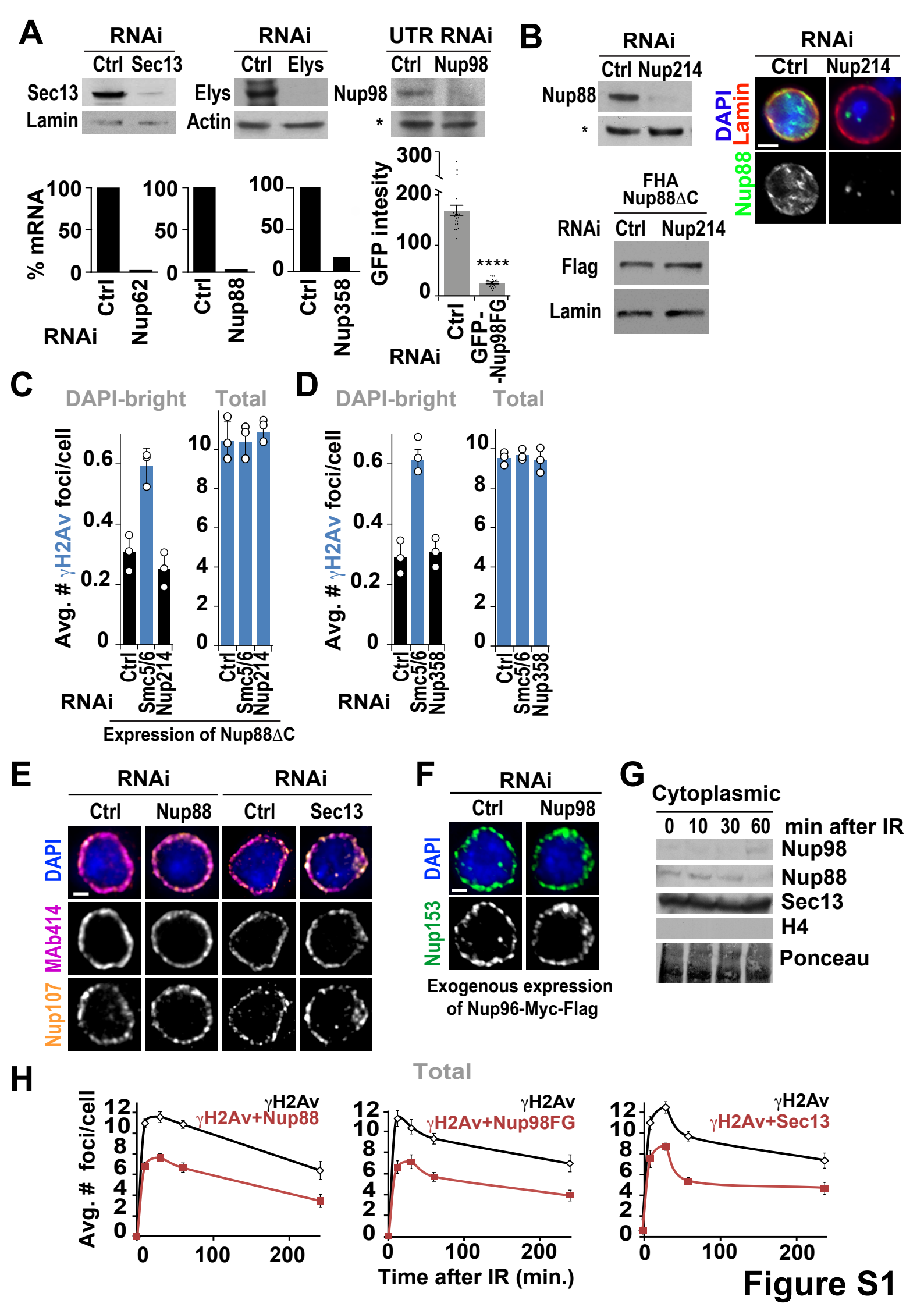
A
RNAi
Ctrl Sec13
Sec13
Lamin
RNAi
Ctrl Elys
Elys
Actin
UTR RNAi
Ctrl Nup98
Nup98
*
% mRNA
100
50
0
Ctrl
Nup62
Nup88
Nup358
RNAi
GFP intesity
300
200
100
0
****
GFP-Nup98FG
B
RNAi
Ctrl Nup214
Nup88
*
DAPI
Lamin
Nup88
FHA Nup88ΔC
RNAi Ctrl Nup214
Flag
Lamin
C
DAPI-bright
Total
Avg. # γH2Av foci/cell
0.6
0.4
0.2
0
10
8
6
4
2
Ctrl
Smc5/6
Nup214
RNAi
Expression of Nup88ΔC
D
Nup358
E
Ctrl Nup88
Ctrl Sec13
DAPI
MAb414
Nup107
F
Ctrl Nup98
Nup153
Exogenous expression of Nup96-Myc-Flag
G
Cytoplasmic
0 10 30 60 min after IR
Nup98
Nup88
Sec13
H4
Ponceau
H
Total
γH2Av
γH2Av+Nup88
γH2Av+Nup98FG
γH2Av+Sec13
Avg. # foci/cell
12
10
8
6
4
2
0
100
200
Time after IR (min.)

Figure S1

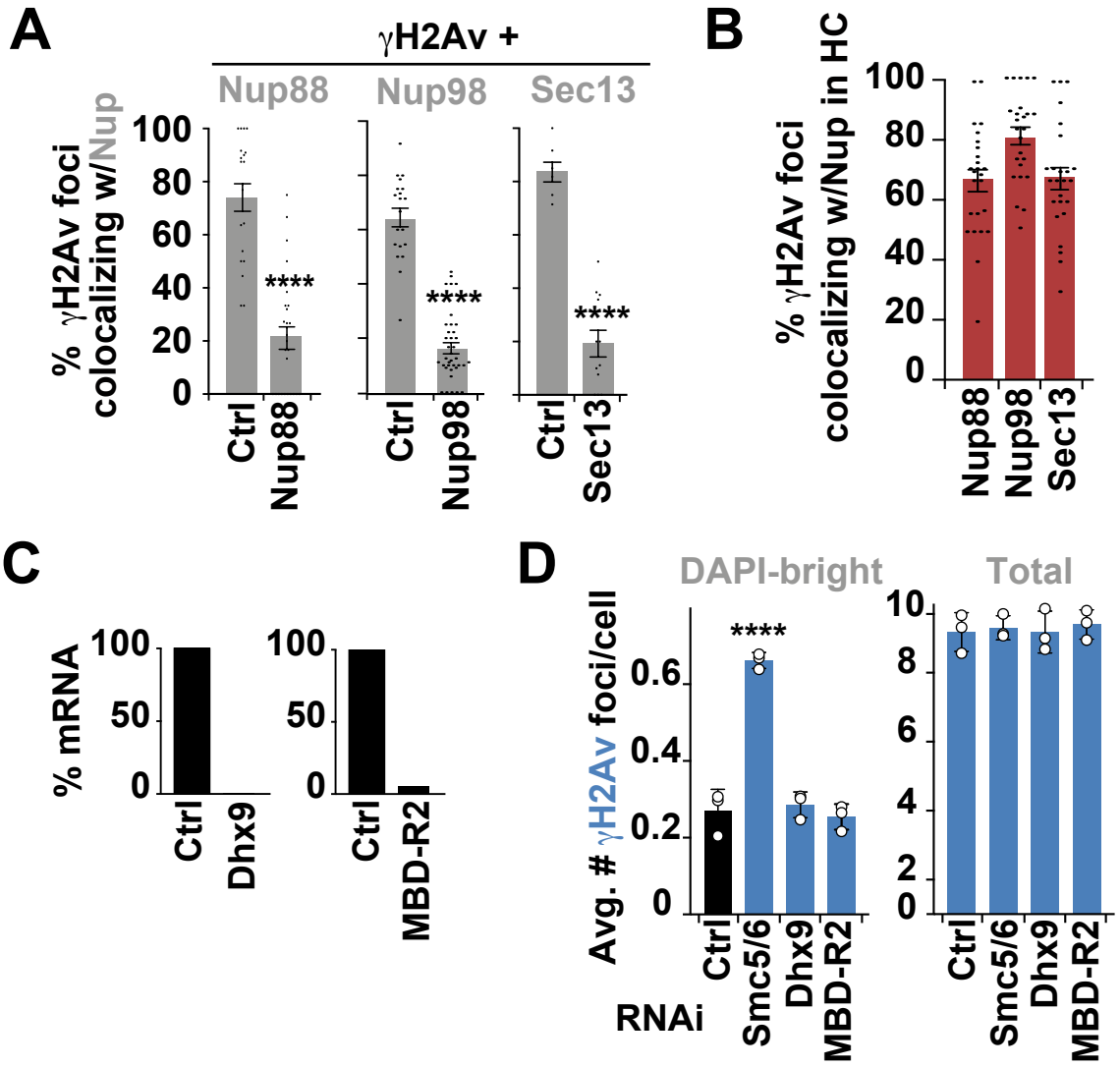
A
γH2Av +
Nup88
Nup98
Sec13
% γH2Av foci colocalizing w/Nup
100
80
60
40
20
0
****
Ctrl
Nup88
Nup98
Sec13
B
% γH2Av foci colocalizing w/Nup in HC
C
% mRNA
50
Dhx9
MBD-R2
D
DAPI-bright
Total
Avg. # γH2Av foci/cell
0.6
0.4
0.2
10
8
6
4
2
RNAi
Smc5/6

Figure S2

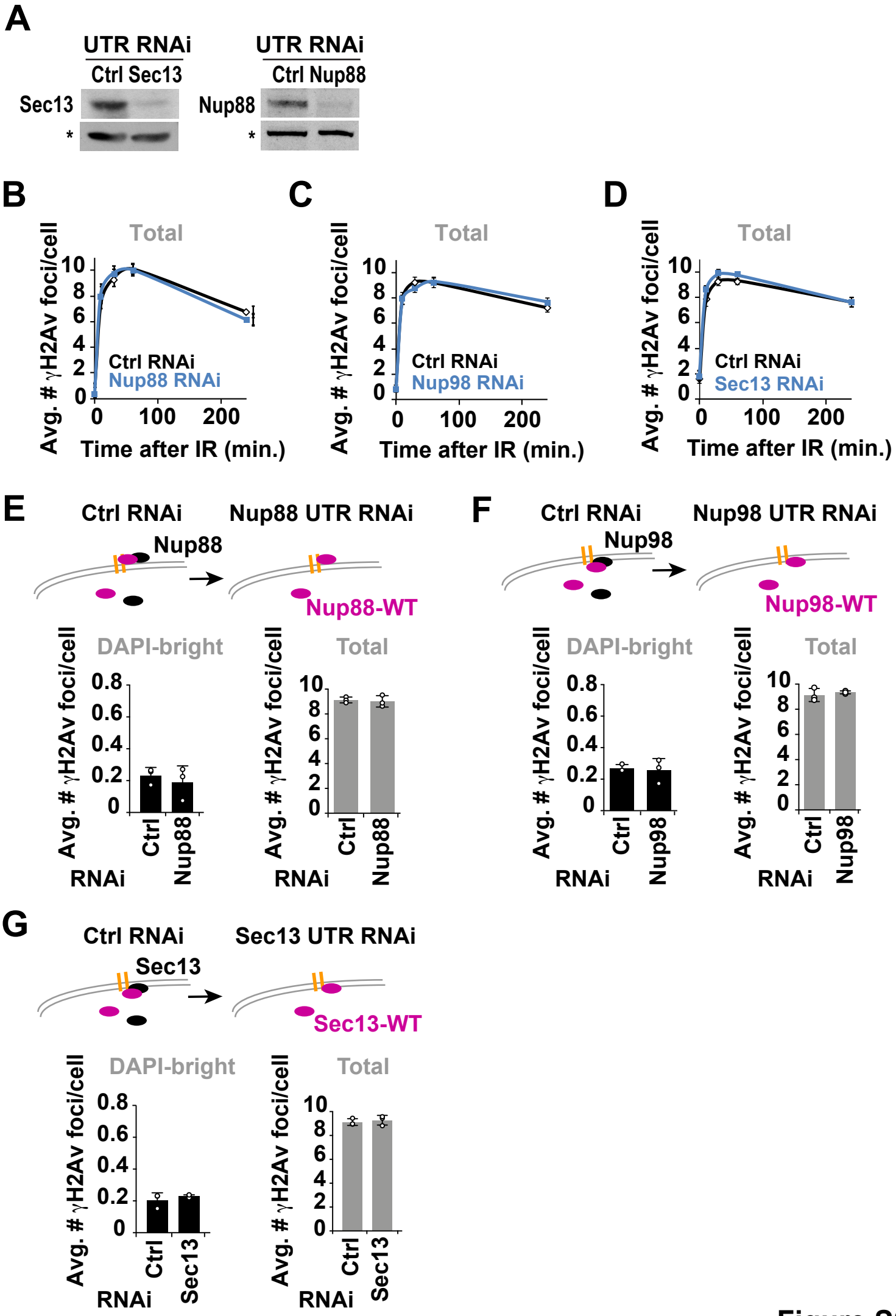
A
UTR RNAi
Ctrl Sec13
Sec13
*
UTR RNAi
Ctrl Nup88
Nup88
*
B
Total
Avg. # γH2Av foci/cell
Ctrl RNAi
Nup88 RNAi
Time after IR (min.)
C
Total
Avg. # γH2Av foci/cell
Ctrl RNAi
Nup98 RNAi
Time after IR (min.)
D
Total
Avg. # γH2Av foci/cell
Ctrl RNAi
Sec13 RNAi
Time after IR (min.)
E
Ctrl RNAi
Nup88 UTR RNAi
Nup88
Nup88-WT
DAPI-bright
Total
Avg. # γH2Av foci/cell
Ctrl
Nup88
RNAi
F
Ctrl RNAi
Nup98 UTR RNAi
Nup98
Nup98-WT
DAPI-bright
Total
Avg. # γH2Av foci/cell
Ctrl
Nup98
RNAi
G
Ctrl RNAi
Sec13 UTR RNAi
Sec13
Sec13-WT
DAPI-bright
Total
Avg. # γH2Av foci/cell
Ctrl
Sec13
RNAi

Figure S3

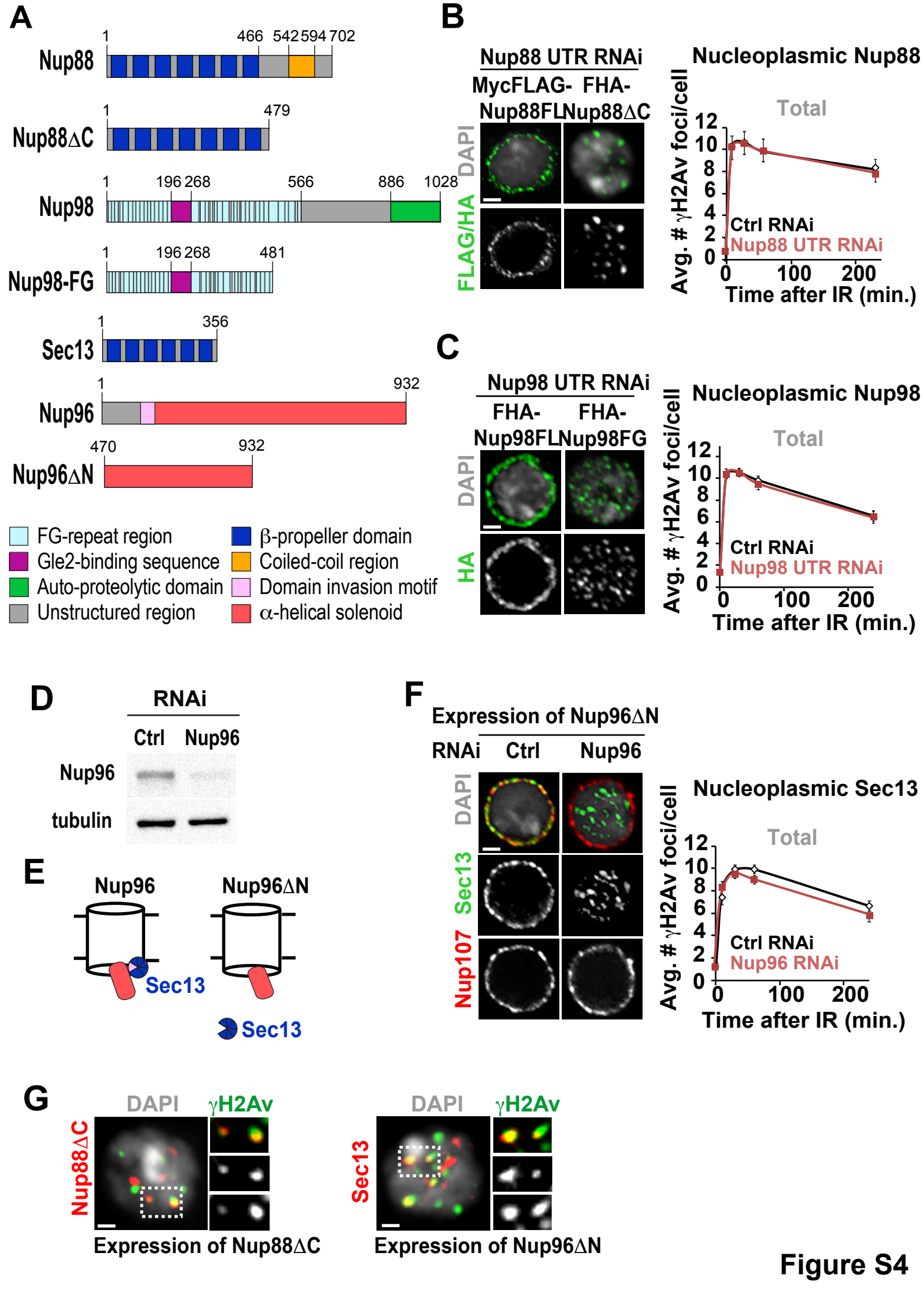
A
Nup88
1
466
542
594
702
Nup88ΔC
1
479
Nup98
1
196
268
566
886
1028
Nup98-FG
1
196
268
481
Sec13
1
356
Nup96
1
932
Nup96ΔN
470
932
FG-repeat region
Gle2-binding sequence
Auto-proteolytic domain
Unstructured region
β-propeller domain
Coiled-coil region
Domain invasion motif
α-helical solenoid
B
Nup88 UTR RNAi
MycFLAG-Nup88FL
FHA-Nup88ΔC
DAPI
FLAG/HA
Nucleoplasmic Nup88
Total
Ctrl RNAi
Nup88 UTR RNAi
Avg. # γH2Av foci/cell
Time after IR (min.)
C
Nup98 UTR RNAi
FHA-Nup98FL
FHA-Nup98FG
DAPI
HA
Nucleoplasmic Nup98
Total
Ctrl RNAi
Nup98 UTR RNAi
Avg. # γH2Av foci/cell
Time after IR (min.)
D
RNAi
Ctrl
Nup96
Nup96
tubulin
E
Nup96
Nup96ΔN
Sec13
Sec13
F
Expression of Nup96ΔN
RNAi
Ctrl
Nup96
DAPI
Sec13
Nup107
Nucleoplasmic Sec13
Total
Ctrl RNAi
Nup96 RNAi
Avg. # γH2Av foci/cell
Time after IR (min.)
G
DAPI
γH2Av
Nup88ΔC
Expression of Nup88ΔC
DAPI
γH2Av
Sec13
Expression of Nup96ΔN

Figure S4

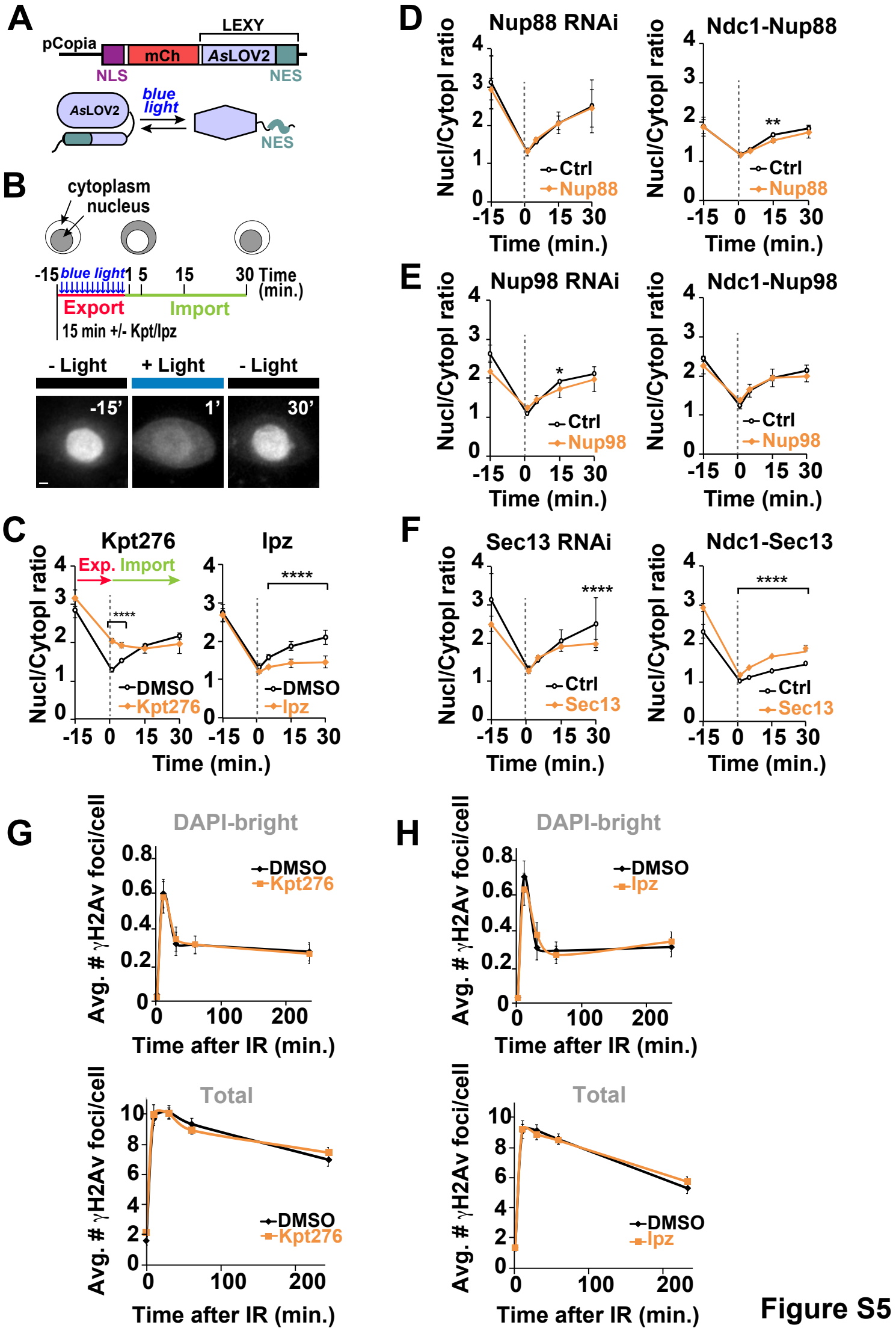
A
pCopia
LEXY
mCh
AsLOV2
NLS
NES
AsLOV2
blue light
NES
B
cytoplasm
nucleus
-15 blue light 1 5 15 30 Time (min.)
Export
Import
15 min +/- Kpt/Ipz
- Light
+ Light
- Light
-15'
1'
30'
C
Kpt276
Ipz
Exp. Import
Nucl/Cytopl ratio
DMSO
Kpt276
Ipz
Time (min.)
D
Nup88 RNAi
Ndc1-Nup88
Ctrl
Nup88
E
Nup98 RNAi
Ndc1-Nup98
Ctrl
Nup98
F
Sec13 RNAi
Ndc1-Sec13
Ctrl
Sec13
G
DAPI-bright
Total
Avg. # γH2Av foci/cell
DMSO
Kpt276
Time after IR (min.)
H
DAPI-bright
Total
DMSO
Ipz

Figure S5

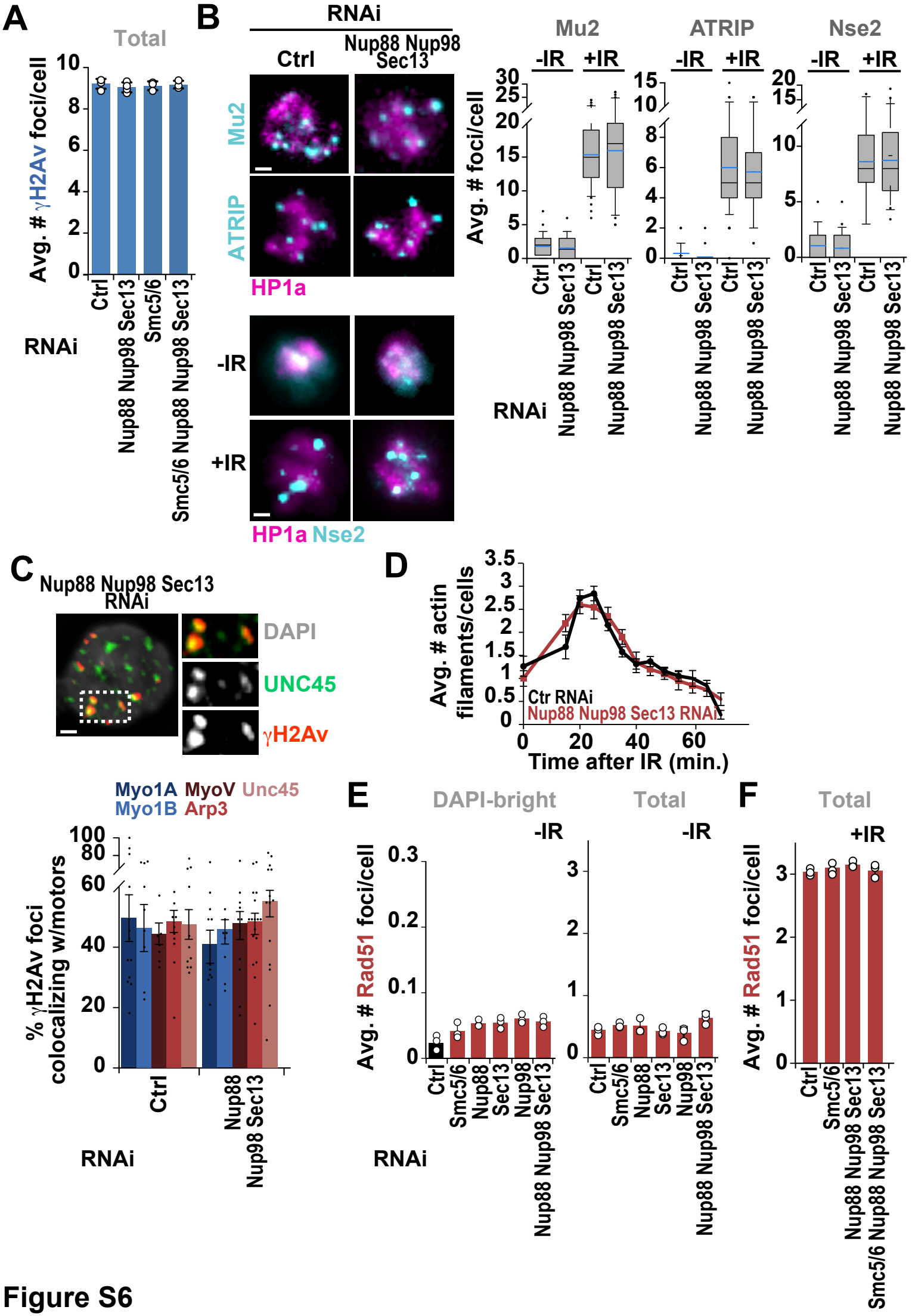
A
Total
Avg. # γH2Av foci/cell
RNAi
Ctrl
Nup88 Nup98 Sec13
Smc5/6
Smc5/6 Nup88 Nup98 Sec13
B
RNAi
Ctrl
Nup88 Nup98 Sec13
Mu2
ATRIP
HP1a
-IR
+IR
HP1a Nse2
Mu2
ATRIP
Nse2
-IR
+IR
Avg. # foci/cell
C
Nup88 Nup98 Sec13 RNAi
DAPI
UNC45
γH2Av
D
Avg. # actin filaments/cells
Ctr RNAi
Nup88 Nup98 Sec13 RNAi
Time after IR (min.)
Myo1A MyoV Unc45
Myo1B Arp3
% γH2Av foci colocalizing w/motors
E
DAPI-bright
Total
Avg. # Rad51 foci/cell
F
Total
+IR

Figure S6

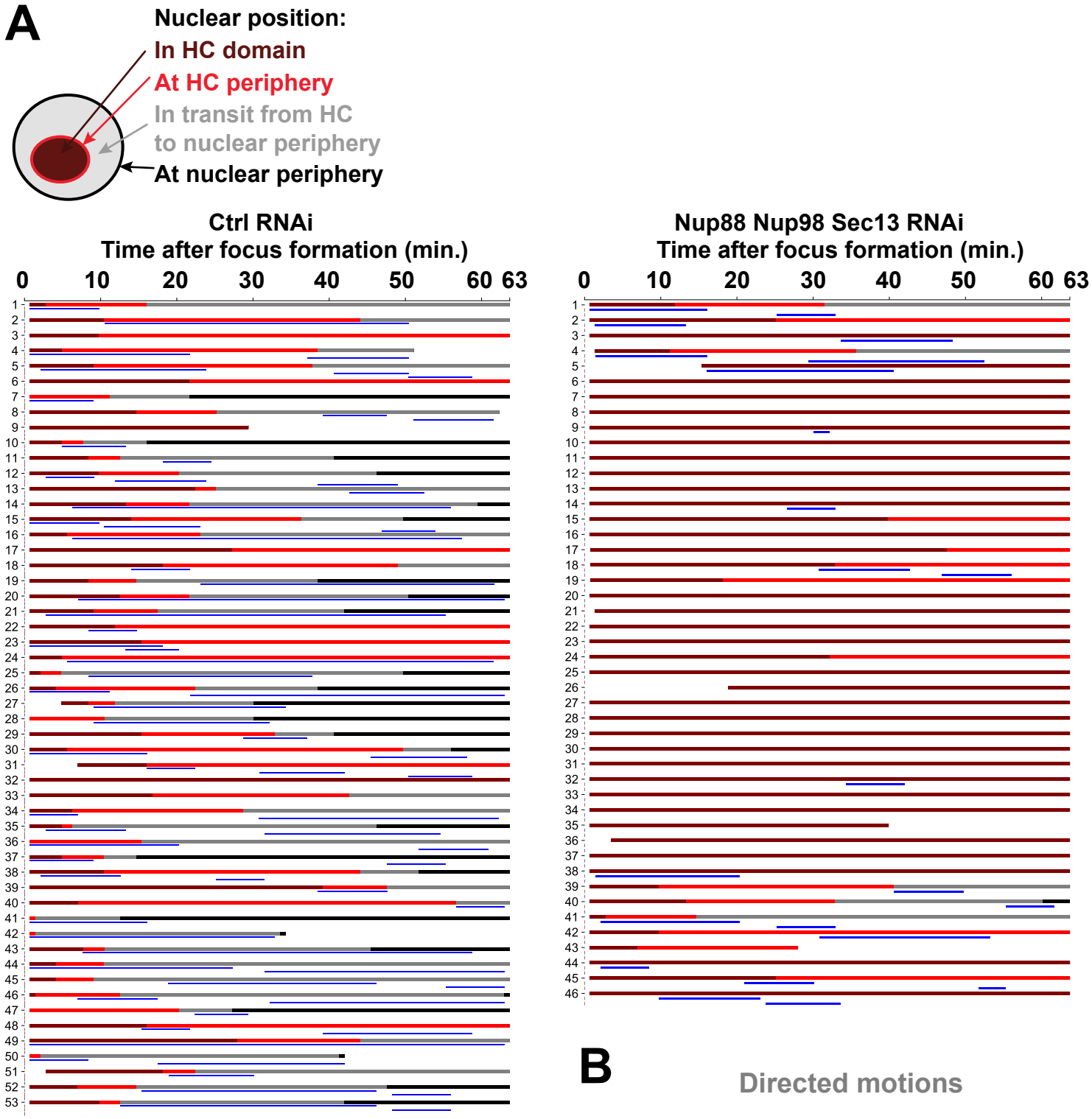
A
Nuclear position:
In HC domain
At HC periphery
In transit from HC
to nuclear periphery
At nuclear periphery
Ctrl RNAi
Time after focus formation (min.)
0 10 20 30 40 50 60 63
Nup88 Nup98 Sec13 RNAi
Time after focus formation (min.)
0 10 20 30 40 50 60 63
B
Directed motions
Ctrl RNAi
Nup88 Nup98
Sec13 RNAi
MSD (μm²)
Δt

Figure S7

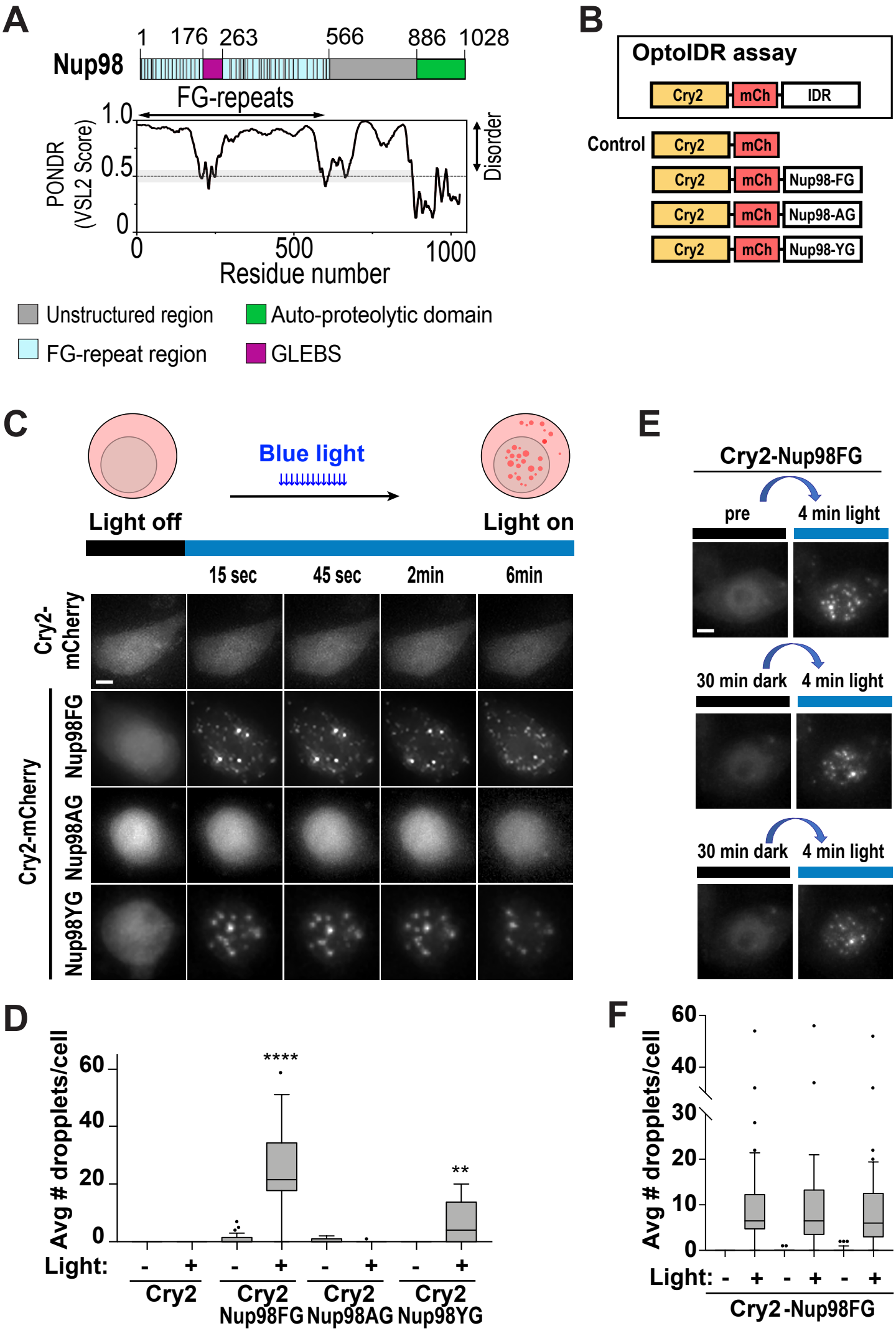
A
Nup98
1
176
263
566
886
1028
FG-repeats
PONDR (VSL2 Score)
1.0
0.5
0
Disorder
0
500
1000
Residue number
Unstructured region
FG-repeat region
Auto-proteolytic domain
GLEBS
B
OptoIDR assay
Cry2
mCh
IDR
Control
Nup98-FG
Nup98-AG
Nup98-YG
C
Blue light
Light off
Light on
15 sec
45 sec
2min
6min
Cry2-mCherry
Nup98FG
Nup98AG
Nup98YG
D
Avg # droppletes/cell
60
40
20
0
****
**
Light:
Cry2
Cry2 Nup98FG
Cry2 Nup98AG
Cry2 Nup98YG
E
Cry2-Nup98FG
pre
4 min light
30 min dark
F
Avg # droppletes/cell
60
40
30
20
10
0
Light:
Cry2-Nup98FG

Figure S8

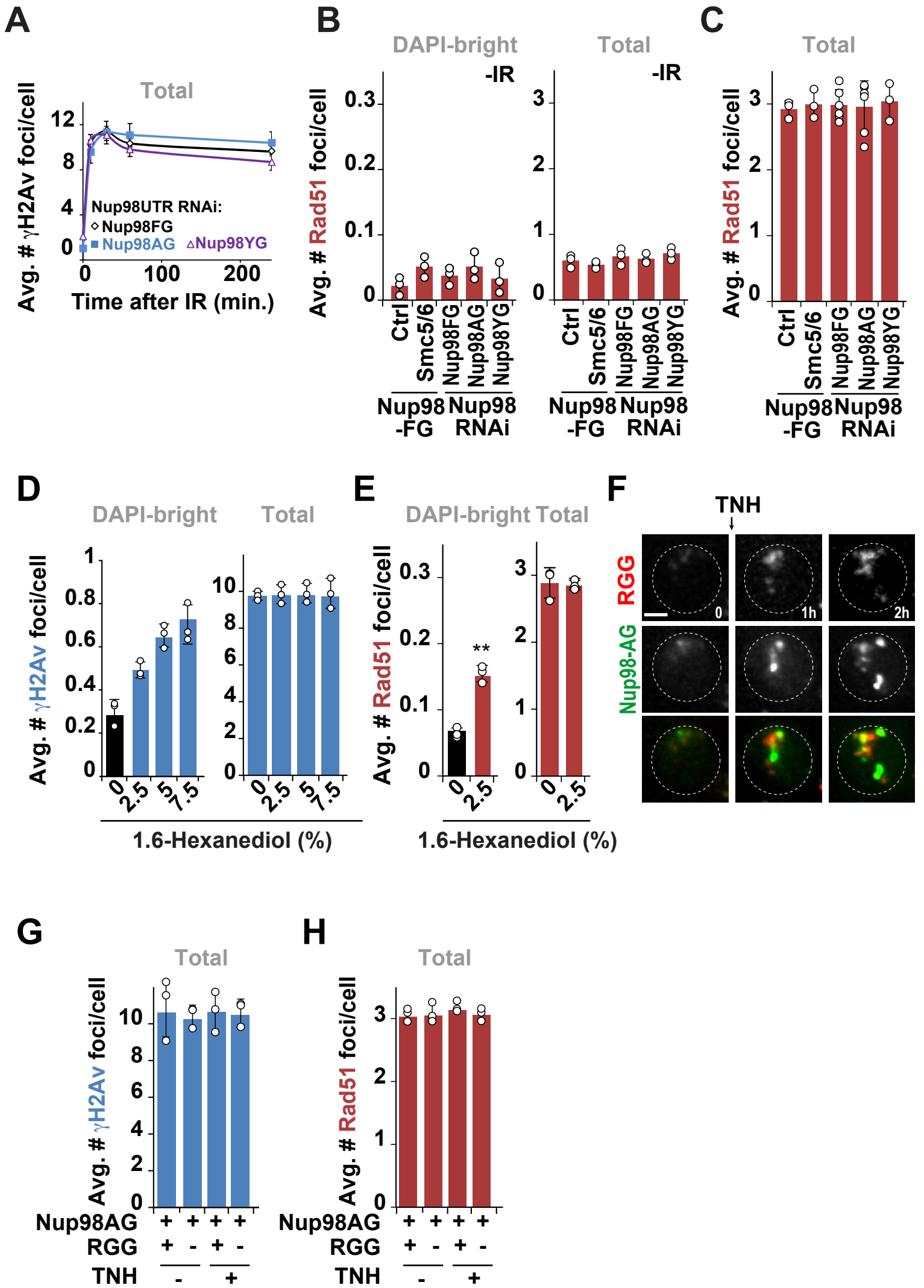
A
Total
Avg. # γH2Av foci/cell
Nup98UTR RNAi:
Nup98FG
Nup98AG
Nup98YG
Time after IR (min.)
B
DAPI-bright
Total
-IR
-IR
Avg. # Rad51 foci/cell
Ctrl
Smc5/6
Nup98FG
Nup98AG
Nup98YG
Nup98 -FG
Nup98 RNAi
C
Total
Avg. # Rad51 foci/cell
D
DAPI-bright
Total
Avg. # γH2Av foci/cell
1.6-Hexanediol (%)
E
DAPI-bright
Total
Avg. # Rad51 foci/cell
**
1.6-Hexanediol (%)
F
TNH
RGG
Nup98-AG
0
1h
2h
G
Total
Avg. # γH2Av foci/cell
Nup98AG
RGG
TNH
H
Total
Avg. # Rad51 foci/cell
Nup98AG
RGG
TNH

Figure S9

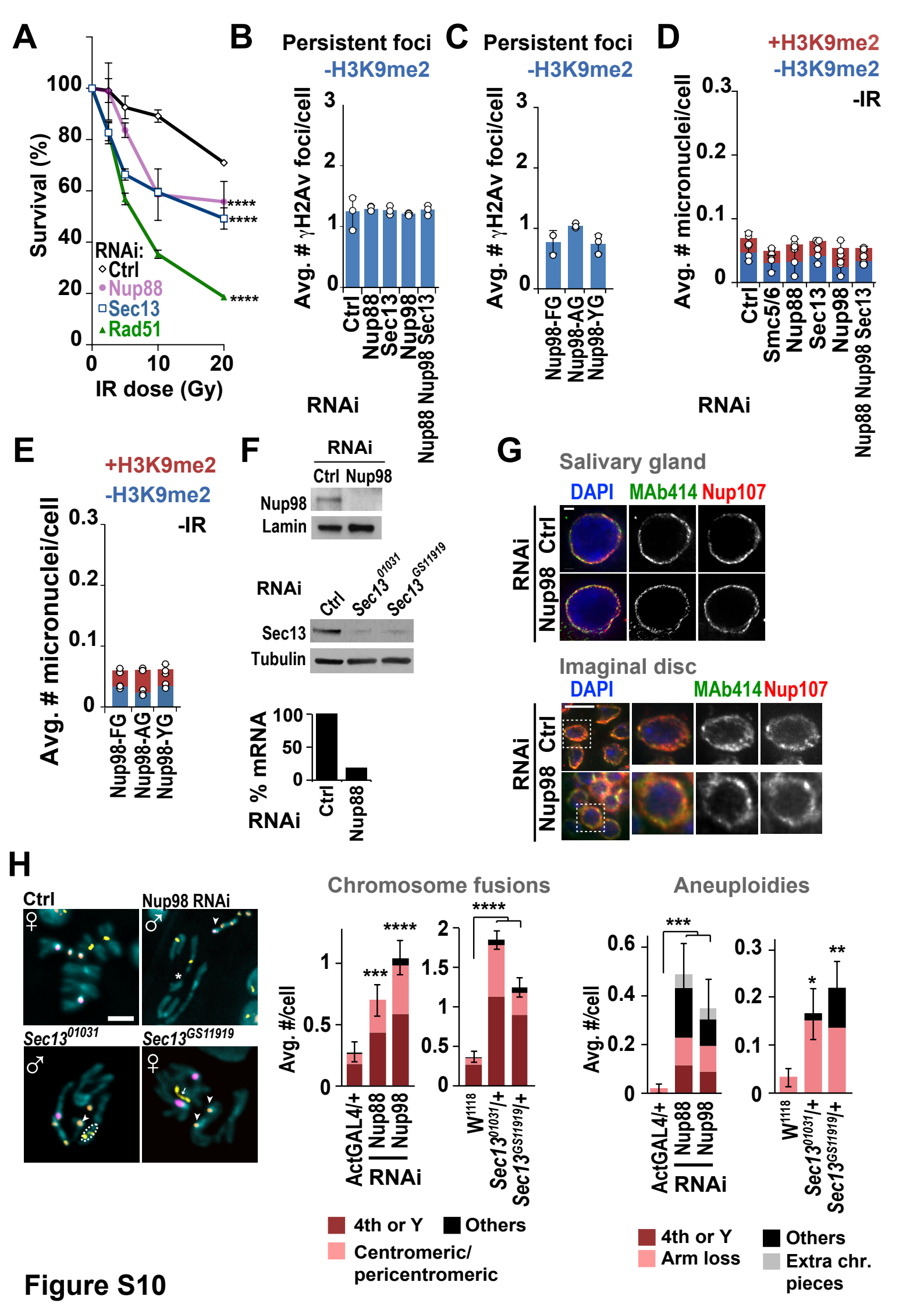
A
Survival (%)
IR dose (Gy)
RNAi:
Ctrl
Nup88
Sec13
Rad51
****
B
Persistent foci
-H3K9me2
Avg. # γH2Av foci/cell
Ctrl
Nup88
Sec13
Nup98
Nup88 Nup98 Sec13
RNAi
C
Persistent foci
-H3K9me2
Avg. # γH2Av foci/cell
Nup98-FG
Nup98-AG
Nup98-YG
D
+H3K9me2
-H3K9me2
-IR
Avg. # micronuclei/cell
Ctrl
Smc5/6
Nup88
Sec13
Nup98
Nup88 Nup98 Sec13
RNAi
E
+H3K9me2
-H3K9me2
-IR
Avg. # micronuclei/cell
Nup98-FG
Nup98-AG
Nup98-YG
F
RNAi
Ctrl Nup98
Nup98
Lamin
RNAi
Ctrl
Sec13 01031
Sec13 GS11919
Sec13
Tubulin
% mRNA
Ctrl
Nup88
RNAi
G
Salivary gland
DAPI
MAb414
Nup107
RNAi
Ctrl
Nup98
Imaginal disc
DAPI
MAb414
Nup107
RNAi
Ctrl
Nup98
H
Ctrl
Nup98 RNAi
Sec13 01031
Sec13 GS11919
Chromosome fusions
Avg. #/cell
ActGAL4/+
Nup88
Nup98
RNAi
W1118
Sec13 01031/+
Sec13 GS11919/+
4th or Y
Others
Centromeric/ pericentromeric
Aneuploidies
Avg. #/cell
ActGAL4/+
Nup88
Nup98
RNAi
W1118
Sec13 01031/+
Sec13 GS11919/+
4th or Y
Arm loss
Others
Extra chr. pieces

Figure S10

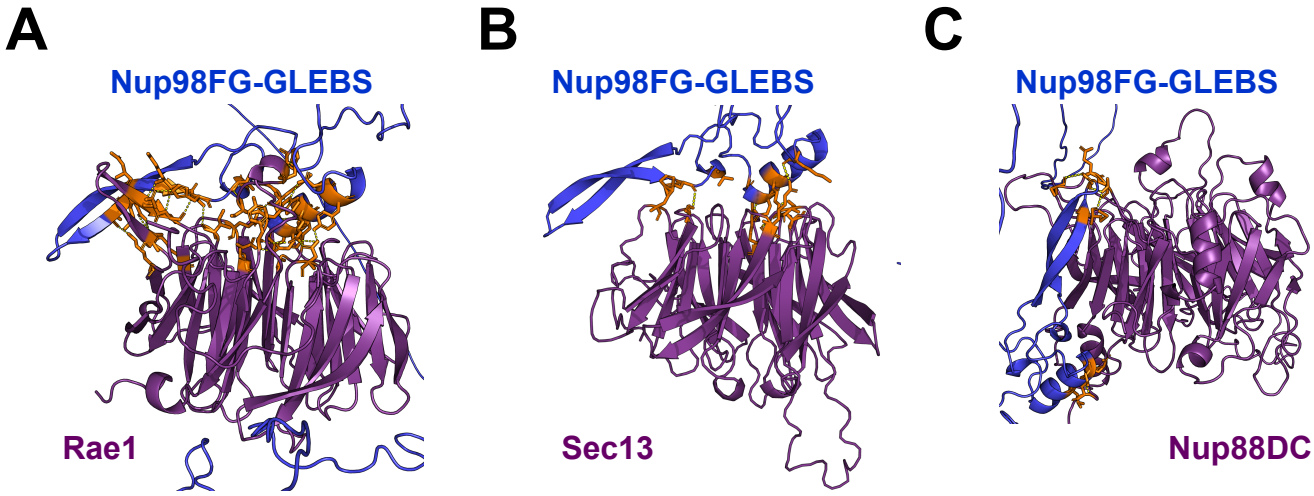
A
Nup98FG-GLEBS
Rae1
B
Nup98FG-GLEBS
Sec13
C
Nup98FG-GLEBS
Nup88DC

Figure S11